

# Where Are the Baryons? II: Feedback Effects

Renyue Cen<sup>1</sup> and Jeremiah P. Ostriker<sup>2</sup>

Received \_\_\_\_\_; accepted \_\_\_\_\_

arXiv:astro-ph/0601008v1 31 Dec 2005

---

<sup>1</sup>Princeton University Observatory, Princeton, NJ 08544; cen@astro.princeton.edu

<sup>2</sup>Princeton University Observatory, Princeton, NJ 08544; jpo@astro.princeton.edu

## ABSTRACT

Numerical simulations of the intergalactic medium have shown that at the present epoch a significant fraction (40 – 50%) of the baryonic component should be found in the ( $T \sim 10^6\text{K}$ ) Warm-Hot Intergalactic Medium (WHIM) - with several recent observational lines of evidence indicating the validity of the prediction. We here recompute the evolution of the WHIM with the following major improvements: (1) galactic superwind feedback processes from galaxy/star formation are explicitly included; (2) major metal species (O V to O IX) are computed explicitly in a non-Equilibrium way; (3) mass and spatial dynamic ranges are larger by a factor of 8 and 2, respectively, than in our previous simulations. Here are the major findings: (1) galactic superwinds have dramatic effects, increasing the WHIM mass fraction by about 20%, primarily through heating up warm gas near galaxies with density  $10^{1.5} - 10^4$  times the mean density. (2) the fraction of baryons in WHIM is increased modestly from the earlier work but is  $\sim 40 - 50\%$ . (3) the gas density of the WHIM is broadly peaked at a density 10 – 20 times the mean density, ranging from underdense regions to regions that are overdense by  $10^3 - 10^4$ . (4) the median metallicity of the WHIM is  $0.18 Z_{\odot}$  for oxygen with 50% and 90% intervals being (0.040,0.38) and (0.0017,0.83).

*Subject headings:* Cosmology: observations, large-scale structure of Universe, intergalactic medium

## 1. Introduction

Cosmological hydrodynamic simulations have strongly suggested that most of the previously “missing” baryons may be in a gaseous phase in the temperature range  $10^5 - 10^7$  K and at moderate overdensity (Cen & Ostriker 1999, hereafter ”CO”; Davé 2001), called the warm-hot intergalactic medium (WHIM), with the primary heating process being hydrodynamic shocks from the formation of large-scale structure at scales currently becoming nonlinear. The reality of the WHIM has now been quite convincingly confirmed by a number of observations from HST, FUSE, Chandra and XMM-Newton (Tripp, Savage, & Jenkins 2000; Tripp & Savage 2000; Oegerle et al. 2000; Scharf et al. 2000; Tittley & Henriksen 2001; Savage et al. 2002; Fang et al. 2002; Nicastro et al. 2002; Mathur, Weinberg, & Chen 2002; Kaastra et al. 2003; Finoguenov, Briel, & Henry 2003; Sembach et al. 2004; Nicastro et al. 2005).

In addition to shock heating, feedback processes following star formation in galaxies can heat gas to the same WHIM temperature range. What is lacking theoretically is a satisfactory understanding of the known feedback processes on the WHIM and how the WHIM may be used to understand and calibrate the feedback processes. Another unsettled issue is how the predicted results will change if one has a more accurate, non-equilibrium calculation of the major metal species, such as O VI, O VII, O VIII, since time scales for ionization and recombination are not widely separated from the Hubble time scale. We have investigated these important processes. Additional improvements include significantly larger dynamic ranges of the simulation, a WMAP normalized cosmological model and an improved radiative transfer treatment. Our current work significantly extends previous theoretical works by our group and others (CO; Davé 2001; Cen et al. 2001; Fang et al. 2002; Chen et al. 2003; Furlanetto et al. 2004,2005a,b; Yoshikawa et al. 2003; Ohashi et al. 2004; Suto et al. 2004; Fang *et al.* 2005). In this paper we focus on the feedback

effects due to star formation and in a companion paper (Cen & Fang 2005) we will present additional effects due to non-equilibrium treatments of metal species and observables of the WHIM. The outline of this paper is as follows: the simulation details are given in §2; in §3 we give detailed results and discussion and conclusions are presented in §4.

## 2. Simulations

Numerical methods of the cosmological hydrodynamic code and input physical ingredients have been described in detail in an earlier paper (Cen et al. 2003). Briefly, the simulation integrates five sets of equations simultaneously: the Euler equations for gas dynamics in comoving coordinates, time dependent rate equations for different hydrogen and helium species at different ionization states, the Newtonian equations of motion for dynamics of collisionless (dark matter) particles, the Poisson equation for obtaining the gravitational potential field and the equation governing the evolution of the intergalactic ionizing radiation field, all in cosmological comoving coordinates. Note that the cosmological (frequency dependent) radiation field is solved for self-consistently, rather than being a separate input to the modeling. The gasdynamical equations are solved using the TVD (Total Variation Diminishing) shock capturing code (Ryu et al. 1993) on a uniform mesh. HI, HeI, HeII are separately followed as different species in a non-LTE rate equations for each cell at every timestep. Oxygen in various states of ionization are also followed as separate species (see Appendix A) and, in total, seven species are followed in non-LTE way. The rate equations are treated using sub-cycles within a hydrodynamic time step due to the much shorter ionization time-scales (i.e., the rate equations are very “stiff”). Dark matter particles are advanced in time using the standard particle-mesh (PM) scheme. A leapfrog scheme integration scheme is used. The gravitational potential on a uniform mesh is solved using the Fast Fourier Transform (FFT) method.

The initial conditions adopted are those for Gaussian processes with the phases of the different waves being random and uncorrelated. The initial condition is generated by the COSMICS software package kindly provided by E. Bertschinger (2001).

Cooling and heating processes due to all the principal line and continuum atomic processes for a plasma of primordial composition with additional metals ejected from star formation (see below), Compton cooling due to the microwave background radiation field and Compton cooling/heating due to the X-ray and high energy background are computed in a time-dependent, non-equilibrium fashion. The cooling due to metals is computed using a code based on the Raymond-Smith code (Raymond, Cox, & Smith 1976) assuming ionization equilibrium (Cen et al. 1995).

We follow star formation using a well defined prescription used by us in our earlier work (Cen & Ostriker 1992,1993) and similar to that of other investigators (Katz, Hernquist, & Weinberg 1992; Katz, Weinberg, & Hernquist 1996; Steinmetz 1996; Gnedin & Ostriker 1997). A stellar particle of mass  $m_* = c_* m_{\text{gas}} \Delta t / t_*$  is created (the same amount is removed from the gas mass in the cell), if the gas in a cell at any time meets the following three conditions simultaneously: (i) contracting flow, (ii) cooling time less than dynamic time, and (iii) Jeans unstable, where  $\Delta t$  is the time step,  $t_* = \max(t_{\text{dyn}}, 10^7 \text{yrs})$ ,  $t_{\text{dyn}} = \sqrt{3\pi / (32G\rho_{\text{tot}})}$  is the dynamical time of the cell,  $m_{\text{gas}}$  is the baryonic gas mass in the cell and  $c_* = 0.07$  is star formation efficiency. Each stellar particle is given a number of other attributes at birth, including formation time  $t_i$ , initial gas metallicity and the free-fall time in the birth cell  $t_{\text{dyn}}$ . The typical mass of a stellar particle in the simulation is about one million solar masses; in other words, these stellar particles are like coeval globular clusters, whose evolution can be computed with standard stellar evolution codes such as those of Bruzual & Charlot (1993). Changing the numerical coefficient  $c_*$  to higher or lower values can change the time dependence of star formation, making it more smooth or more “bursty”

but has little effect on the total mass in stars/galaxies or in the overall simulation. All variations of this commonly adopted star-formation algorithm essentially achieve the same goal: in any region where gas density exceeds the stellar density, gas is transformed to stars on a timescale longer than the local dynamical time and shorter than the Hubble time. Since these two time scales are widely separated, the effects, on the longer time scale, of changing the dimensionless numbers (here  $c_*$ ) are minimal. Since nature does not provide us with examples of systems which violate this condition (systems which persist over many dynamical and cooling time scales in having more gas than stars), this commonly adopted algorithm should be adequate even though our detailed understanding of star formation remains primitive.

Stellar particles are treated dynamically as collisionless particles subsequent to their birth. But feedback from star formation is allowed in three forms: ionizing UV photons, the effects of the cumulative SN explosions and AGN output known as Galactic Superwinds (GSW), and metal-enriched gas, all being proportional to the local star formation rate. The temporal release of all three feedback components at time  $t$  has the same form:  $f(t, t_i, t_{dyn}) \equiv (1/t_{dyn})[(t - t_i)/t_{dyn}] \exp[-(t - t_i)/t_{dyn}]$ . Within a time step  $dt$ , the released GSW energy to the IGM, ejected mass from stars into the IGM and escaping UV radiation energy are  $e_{GSW}f(t, t_i, t_{dyn})m_*c^2dt$ ,  $e_{mass}f(t, t_i, t_{dyn})m_*dt$  and  $f_{esc}(Z)e_{UV}(Z)f(t, t_i, t_{dyn})m_*c^2dt$ . We use the Bruzual-Charlot population synthesis code (Bruzual & Charlot 1993; Bruzual 2000) to compute the intrinsic metallicity-dependent UV spectra from stars with Salpeter IMF (with a lower and upper mass cutoff of  $0.1 M_\odot$  and  $125 M_\odot$ ). Note that  $e_{UV}$  is no longer just a simple normal coefficient but a function of metallicity. The Bruzual-Charlot code gives  $e_{UV} = (1.2 \times 10^{-4}, 9.7 \times 10^{-5}, 8.2 \times 10^{-5}, 7.0 \times 10^{-5}, 5.6 \times 10^{-5}, 3.9 \times 10^{-5}, 1.6 \times 10^{-6})$  at  $Z/Z_\odot = (5.0 \times 10^{-3}, 2.0 \times 10^{-2}, 2.0 \times 10^{-1}, 4.0 \times 10^{-1}, 1.0, 2.5, 5.0)$ . We also implement a gas metallicity dependent ionizing photon escape fraction from galaxies in the sense that

higher metallicity, hence higher dust content, galaxies are assumed to allow a lower escape fraction; we adopt the escape fractions of  $f_{esc} = 2\%$  and  $5\%$  (Hurwitz et al. 1997; Deharveng et al. 2001; Heckman et al. 2001; Steidel et al. 2001; Shapley et al. 2005) for solar and one tenth of solar metallicity, respectively, and interpolate/extrapolate using a linear log form of metallicity. In addition, we include the emission from quasars using the spectral form observationally derived by Sazonov, Ostriker, & Sunyaev (2004), with a radiative efficiency in terms of stellar mass of  $e_{QSO} = 2.5 \times 10^{-5}$  for  $h\nu > 13.6\text{eV}$ . This number,  $e_{QSO}$ , convolves together the ratio of black hole mass to stellar mass,  $\sim 1 \times 10^{-3}$  (Kormendy & Gebhardt 2001), the radiative efficiency of black holes 0.1 (Yu & Tremaine 2002) and the fraction of the radiative energy emitted beyond the Lyman limit 0.25 (Sazonov et al. 2004). Finally, hot, shocked regions (like clusters of galaxies) emit ionizing photons due to bremsstrahlung radiation, which are also included. The UV component is simply averaged over the box, since the light propagation time across our box is small compared to the time steps. The radiation field (from 1eV to 100keV) is followed in detail with allowance for self-consistently produced radiation sources and sinks in the simulation box and for cosmological effects, i.e., radiation transfer for the mean field  $J_\nu$  is computed with stellar, quasar and bremsstrahlung sources and sinks due to Ly $\alpha$  clouds etc (Equation 7 of Cen 1992). In addition, a local optical depth approximation is adopted to crudely mimic the local shielding effects: each cubic cell is flagged with six hydrogen “optical depths” on the six faces, each equal to the product of neutral hydrogen density, hydrogen ionization cross section and scale height, and the appropriate mean from the six values is then calculated; equivalent ones for neutral helium and singly-ionized helium are also computed. In computing the global sink terms for the radiation field the contribution of each cell is subject to the shielding due to its own “optical depth”. In addition, in computing the local ionization and cooling/heating balance for each cell the same shielding is taken into account to attenuate the external ionizing radiation field.

It is very difficult to accurately model the effects of GSW. A proper treatment would include allowance for a multiphase medium having most of the mass in clouds or filaments occupying a small fraction of the volume. Significant progress has been made recently to provide a better treatment of the multi-phase interstellar medium (Yepes et al. 1997; Elizondo et al. 1999a,b; Hultman & Pharasyn 1999; Ritchie & Thomas 2001; Springel & Hernquist 2003) but the generation of GSW is far from being adequately modeled. Clearly, a combination of both high resolution and detailed multi-phase medium treatment (including magnetic fields and cosmic rays) is requisite before our understanding of the interactions between galaxy formation and IGM can be considered to be truly satisfactory. This problem is too difficult for us to address with our code, so we have chosen to not attempt to calculate the *causes* and generation of GSW, but, instead, to simply assume an input level of mass, energy and metals, and carefully compute the *consequences* of GSW on the surrounding medium. For this purpose our code is very well designed.

Thus, GSW energy and ejected metals are distributed into 27 local gas cells centered at the stellar particle in question, weighted by the specific volume of each cell. We fix  $e_{mass} = 0.25$ , i.e., 25% of the stellar mass is recycled. GSW energy injected into the IGM is included with an adjustable efficiency (in terms of rest-mass energy of total formed stars) of  $e_{GSW}$ , which is normalized to observations for our fiducial simulation with  $e_{GSW} = 3 \times 10^{-6}$ . If the ejected mass and associated energy propagate into a vacuum, the resulting velocity of the ejecta would be  $(e_{GSW}/e_{mass})^{1/2}c = 1470\text{km/s}$ . After the ejecta has accumulated an amount of mass comparable to its initial mass, the velocity may slow down to a few hundred km/s. We find that this velocity roughly corresponds to the observed outflow velocities of LBGs (e.g., Pettini et al. 2002). We also make simulations with no GSW and with stronger GSW to investigate the effects of GSW on IGM. Thus all the uncertainties concerning how much of the energy which is generated by feedback can escape into the surrounding IGM is encapsulated into one parameter  $e_{GSW}$ .



The results reported on here are based on new simulations of a *WMAP*-normalized (Spergel et al. 2003; Tegmark et al. 2004) cold dark matter model with a cosmological constant,  $\Omega_M = 0.31$ ,  $\Omega_b = 0.048$ ,  $\Omega_\Lambda = 0.69$ ,  $\sigma_8 = 0.89$ ,  $H_0 = 100h\text{kms}^{-1}\text{Mpc}^{-1} = 69\text{kms}^{-1}\text{Mpc}^{-1}$  and  $n = 0.97$ . The adopted box size is  $85\text{Mpc}/h$  comoving and with a number of cells of  $1024^3$ , the cell size is  $83\text{kpc}/h$  comoving, with dark matter particle mass equal to  $3.9 \times 10^8 h^{-1} M_\odot$ . Given a lower bound of the temperature for almost all the gas in the simulation ( $T \sim 10^4$  K), the Jeans mass  $\sim 10^{10} M_\odot$  for mean density gas, which is comfortably larger than our mass resolution.

### 3. Results

As in CO, in our analysis we divide the IGM into three components by temperature: (1)  $T > 10^7\text{K}$  (the normal X-ray emitting gas, predominantly in collapsed and virialized clusters of galaxies); (2)  $10^7 \text{ K} > T > 10^5 \text{ K}$  gas, which is defined as WHIM and exists mainly in unvirialized regions; (3)  $T < 10^5 \text{ K}$  warm gas, which is mostly in low density regions. A last component (4) is the cold gas that has been condensed into stellar objects, which we designate “galaxies”, and which will contain stars and cold gas. After reionization at  $z \sim 6$  (e.g., Gnedin & Ostriker 1997; Fan et al. 2002; Cen & McDonald 2002), driven by the absorption of UV photons from the early generation of stars and quasars, the photoionized IGM is left in the “warm” component with  $T \sim 10^{4.0-4.3}$  K. Then, as larger and larger scale structure forms, the breaking waves of wavelength  $\lambda_{NL}(t)$  cause gas to shock heat to temperatures  $\frac{kT(t)}{\mu m_p} = A[\lambda_{NL}(t)H(t)]^2$ , which increases monotonically with time, where  $H(t)$  is the Hubble constant at time  $t$ . Details of this fit were provided in CO ( $A \sim 3/16$ ). Thus, warm gas is increasingly shock heated, removed from that category and added to the WHIM category with the shocks forming the observed filamentary network seen in Figure 2. By redshift  $z \sim 2$ ,  $\lambda_{NL}$  has increased to the point where, at the nodes,

where filaments intersect, gas has been shocked into the “hot” X-ray emitting gas category as we begin to see the formation of the great clusters of galaxies in these regions. While not expected to be the primary heater of IGM, GSW from star forming galaxies are observed to blow winds at speeds of several hundred kilometers per second and will heat up IGM, in the vicinity of galaxies.

Figure 1 shows the evolution of these four components. We note that 49% of all baryons are in WHIM by the time  $z = 0$ , which is consistent with our previous findings (CO). Without galactic superwinds the mass fraction in WHIM is reduced from  $\sim 50\%$  to  $\sim 40\%$ , which may partially explain lower WHIM mass fractions in other simulations without galactic superwinds as found in Davé et al. (2001). The bottom line is this: while galactic superwinds are subdominant to gravitational heating caused by the collapse of large-scale density waves, they make, nevertheless, about a 20% contribution to the overall WHIM mass. Other components are consistent with our earlier results and approximately in agreement with observations with regard to low- $z$  redshift Ly $\alpha$  cloud gas (Penton, Stocke, & Shull 2004), X-ray clusters of galaxies and stellar mass (Fukugita, Hogan, & Peebles 1998).

The hot component gas reached 11% in this simulation by  $z = 0$ , which is somewhat smaller than the 19% found in our previous work (CO). The difference is partly due to difference in the model parameters and partly due to cosmic variance. This component is not greatly affected by GSW (cf. Figure 13c). As noted, our attention will be focused in this paper on the WHIM (solid dots) in Figure 1b: the warm/hot gas rises dramatically in abundance with increasing time and dominates the mass balance by  $z = 0$ , reaching 49% of the total baryons. Therefore, our new simulations with a host of improved physical treatments and numerical details confirm our previous results: the long sought missing baryons (those not seen in the more easily observed warm and hot components) should

be found in the WHIM. The primary purpose of this paper is, in addition, to provide a more quantitative description of the observable properties of the WHIM to better test this prediction.

All subsequent results are focused on redshift zero. The characteristic spatial distribution of the WHIM is shown in Figure 2. We see again a filamentary structure (in green) as found previously (CO) where, at the high density nodes (red), “galaxies” as well as very hot gas have been collected to form X-ray bright clusters of galaxies. This “Cosmic Web” is traced out by moderate density gas (the green filaments); galaxies and other virialized objects are beads threading the green filaments. The vast volume between the filaments is mostly underdense in gas, which is also relatively devoid of galaxies (Peebles 1999).

Figure 3 shows the gas distribution in the density-temperature plane. The gas in this phase space can be best described using the four baryon components defined in the beginning of this section. First, one sees a cooling feature at  $T \sim 10^4$  K and overdensity  $\sim 10^{3.5-5.0}$ , where the gas is cooling rapidly to form stars. Second, the lower left corner in the plot ( $\rho \leq 1$  and  $T < 10^4$  K) represents cold-warm gas in the voids which does not cool efficiently via radiative processes but cools adiabatically due to the expansion of the universe after initial photoionization and photoheating. Third, both WHIM and hot gas are heated up primarily by shocks formed during large-scale structure formation. Initially, this heated gas tends to occupy the upper right corner of the phase space, representing relatively dense regions that have attained high temperature due to shocks, some of which are in virialized regions corresponding to groups and clusters of galaxies. With time the shocks continue to expand and propagate into lower density regions when matter continues to infall towards these regions, resulting in the mass concentration contours in Figure 3 moving to the left in the displayed phase space and filling up the upper left quarter of the

plot. We provide a fitting formula that traces the locus of the ridge line in the  $T - \rho$  plane for the WHIM as:

$$\log(T) = 8 - [4(\log \rho_g / \bar{\rho}_g)^{0.9}]^{-1}, \quad (1)$$

where  $T$  is in the range  $10^5 - 10^7$  K and  $\rho_g$  is gas density and  $\bar{\rho}_g$  is the mean gas density  $z = 0$ .

Comparing the top and bottom panels in Figure 3, we see that, while the overall effect of GSW on the IGM is significant as shown in Figure 1b, it is not easily discernible here quantitatively. However, one feature is very noticeable even to the eye: it is clearly seen that in the simulation with galactic superwinds some gas in IGM is being pushed towards the left (near the upper left corner) in the WHIM temperature range in the plot. This suggests that GSW visibly propagate into lower density regions.

Before presenting detailed quantitative calculations of the GSW effects, we provide a more pictorial view of the GSW processes. Figures 4-9 provide a close-up view of a region of size  $21.2 \times 21.2 \text{Mpc}^2/h^2$  and thickness of  $1.75 \text{Mpc}/h$  that has had significant GSW activity in the recent past. We note that, as shown in Cen, Nagamine & Ostriker (2005), GSW effects tend to be more vigorous at higher redshifts when star formation rate was higher. Nevertheless, the GSW effects on the surrounding IGM are strongly visible even at  $z = 0$ . Figure 4 compares the gas density distributions in the two simulations without and with GSW, respectively. Overall, the effect on the appearance of large-scale density structure by GSW is small and its effect on low density regions (blue and purple regions) is negligible, simply because GSW do not reach there or, they turn very weak even if reaching there. The effect on high density regions ( $> 10^2$ ; yellow regions) is quite visible, in the sense that GSW tend to suppress the gas density concentration in these regions and disperse gas outwards, noting that some of the yellow spots in the simulation without GSW are significantly suppressed; examples include the features at  $(8, 5) \text{Mpc}/h$ ,  $(13, 8) \text{Mpc}/h$  and  $(6, 13) \text{Mpc}/h$ .

This effect will be quantified more precisely in subsequent figures.

Figure 5 shows the temperature distribution in the same slice for simulations without and with GSW, respectively. We see that large-scale gravitational collapse induced shocks tend to center on dense regions; these are virialization and infall shocks due to gravitational collapse of high density peaks. Some of the larger peaks are seen to be enclosed by shocks of temperature in excess of  $10^7$  K (note that the displayed picture is inevitably subject to smoothing by projection thus the higher temperature regions have their temperatures somewhat underestimated). A few shock structures are clearly caused by GSW, however, because they appear prominent only in the simulation with GSW; for example, in the upper left quarter, the NW-SE oriented gravitational shock feature near  $(6, 14)$ Mpc/h, which is aligned with a high density filament (see Figure 4), is significantly enlarged by GSW shocks propagating approximately in the direction (NE-SW) perpendicular to the filament. The resulting shock temperature is in the WHIM temperature range of  $10^5 - 10^7$  K. Another large feature is seen in the lower right quarter near  $(18, 5)$ Mpc/h in the simulation with GSW, which is nearly invisible in the simulation without GSW; this feature is most likely produced by a GSW shock originating from a galaxy not centrally located in the displayed slice, since there is no significant density concentration at that location in Figure 4. These regions affected by GSW clearly are heating up regions of warm gas and its surroundings seen in Figures 4,5 and adding this gas to the WHIM; more quantitative results are given later.

Figure 6 shows the metals density distribution in the same slice for simulations without and with GSW, respectively. The most visible difference between simulations with and without GSW is that the high metallicity (yellow) regions in the close vicinity of galaxies are substantially extended by GSW. This is because metals in the case of no GSW are concentrated in regions of about our grid size and the GSW cause these extremely dense

metal nuggets to appear on the IGM scale. The predicted effect has perhaps received dramatic confirmation in the O VI absorption measurements of Stocke et al. (2005), where they find that O VI absorbers are invariably found with 800 kpc of galaxies. The affected regions have a size of a few hundred kiloparsecs to about one megaparsec, suggesting that this is the range of influence of GSW in transporting metals to the IGM. It is noted that the shocks, seen in Figure 5, tend to propagate further out to scales of  $1 - 2\text{Mpc}/h$ , while apparently leaving metals significantly behind, i.e., the energy of the GSW is as expected transported more efficiently than metals. As we will show quantitatively later, heating metal-rich warm gas and significant dispersal of heated-up WHIM gas to significant distances from galaxies is the most dramatic role played by GSW. Most spectacularly, GSW reduces the total amount of metals in cold-warm gas in the close vicinity of galaxies by a factor of 3 compared to the case without GSW and adds all this metal-enriched gas to WHIM.

Figure 7 compares the non-LTE-computed O VI density for the simulations without and with GSW, respectively. The visibly discernible difference caused by GSW is that GSW tend to disperse concentrations of O VI density, in accordance with overall metals dispersal in dense regions seen in Figures 6, and tend to create typically non-spherical features in the immediate regions surrounding galaxies on the scales of  $< 1\text{Mpc}$ . The differences caused by GSW on O VII density shown in Figure 8 appear to be somewhat larger than those for O VI density, suggesting that GSW heated regions around galaxies are more often in the range of  $10^6 - 10^7$  K, higher than optimal temperature of  $10^{5.5}$  K for O VI, which seems to be consistent with Figures 5. This is confirmed by Figure 9 where O VIII density is shown for simulations without and with GSW, respectively. The overall results from Figures 4-9 indicate that the effects of GSW on the abundances of individual species can not be easily described and the only means to compare models and observations is via direct simulations. This is because the relative abundance of an individual species depends on

the temperature and density history of the gas, which in turn would depend on the shock (i.e., GSW) strengths and environments, which are too complicated to be characterized by simple analytically tractable relations.

Clearly, the regions where differences caused by GSW are visible to the eye in Figure 3 do not contain a significant amount of IGM mass. More dense regions must have been affected by galactic superwinds to account for the effect indicated in Figure 1b, which are visually confirmed by the pictures shown above. We quantify this further to have a better understanding. Figures 10,11,12 show the concentration of gas mass of the three IGM components, warm, WHIM and hot, respectively, in the dark matter density-gas density plane. Comparing the simulations with (solid contours) and without (dashed contours) GSW reveals some important information. From Figure 10 we see that there are two separate mass concentrations for the warm IGM component, one centered at about the mean density and the other at about  $10^3$  times the mean density. The physical nature of these two separate concentration is quite clear, as noted earlier: the peak at the lower density is primarily photo-heated gas in the voids, whereas the peak at the high density is the cooled gas reservoir for star formation. The effect of GSW seems to push the peak at the lower density to the left, i.e., some gas in low-to-moderate density is being pushed to slightly lower (dark matter) density regions by GSW. This is quite understandable. The peak at the high density, however, appears to move both left and down-left with GSW. This may be understood by two cases that may be occurring simultaneously. First, as in the previous case, gas is simply blown out of high density regions, causing it to move left. Second, for some regions where gas density has become comparable to or larger than the dark matter density due to gas cooling and condensation, reduction in gas density due to GSW would have dynamic effects on both the remaining gas and the dark matter, resulting in a gravitational potential change, which may explain the down-left movement of the contour peak. Since the high density regions provide the gas reservoir for star formation,

GSW is explicitly shown here to have a major effect on reducing and regulating star formation, which is verified by the reduced (but adequate) star formation in the simulation with GSW that appears to be consistent with observations (Fukugita, Hogan & Peebles 1998); the total stellar mass density at  $z = 0$  is  $\Omega_* = 0.0037$ , as compared to 0.006 in the simulation with GSW.

The effect of GSW on the WHIM is shown in Figure 11. Since most of the mass in WHIM is in regions with moderate density (10 – 20 times the mean density), the dark matter dominates the gravitational potential. Therefore, the primary effect of the GSW on WHIM is in moving gas into somewhat lower density regions and heating up gas in regions with a wide range of densities, as shocks sweep through them in the direction of negative density gradient. The same effect is seen for the hot component (Figure 12), although the overall effect is somewhat diminished, simply because the incremental increase in energy due to GSW in these regions is subdominant to the gravitational potential energy, released in strong shocks.

Figure 13 summarizes more quantitatively the trends in Figures 10,11,12, in a slightly different way, where the probability distribution of each of the three gas components is shown as a function of the gas density. The most dramatic difference is seen for the warm component (dotted curves in the top panel) between simulations with (thick dotted curve) and without (thin dotted curve) GSW. We see that a substantial fraction of the warm gas at density  $\rho / \langle \rho_b \rangle = 10^{1.3} - 10^{4.5}$  is removed by GSW. This removed gas from the warm component is primarily added to the WHIM gas, as clearly indicated by the difference for WHIM components between simulations with (thick solid curve) and without (thin solid curve) GSW. And there is an overall shift of this component to lower densities where radiative cooling would be less efficient. The effect of GSW on the hot component is rather small, as seen by the nearly overlapping thick dashed curve and thin dashed curve in the



bottom panel. Figure 14 demonstrates in a different way the same point: the gain in WHIM fraction is at the expense of warm gas, heated up by GSW.

Metals originated in galaxies are transported by GSW and other hydrodynamic/gravitational processes. The role that GSW actually play to affect the distribution of metals in the IGM are complex. Figure 15 shows the distribution of metals in each of the three IGM components as a function of metallicity. The warm component displays a bimodal distribution with one peak at high metallicity corresponding to the star formation regions, while the other peak at very low metallicity corresponding to the uncontaminated, predominantly low density, regions remote from late time star formation regions and a relic from very early low mass galaxy formation. It is stressed that the exact metallicity value of the the lower metallicity peak is very uncertain, significantly subject to resolution effects; it is likely that our still relatively poor resolution must have underestimated star formation at high redshift in quite small galaxies not well resolved by our numerical resolution, which may otherwise have enriched the IGM with metals to a higher floor level. In addition, the metals produced by the very first generation of stars (e.g., Cen 2003; Ricotti & Ostriker 2004) may also help to have raised the metallicity floor in the IGM. Overall, the effect of GSW is to reduce the amount of metals in the high metallicity peak ( $Z \sim 0.3$  to  $1.0 Z_{\odot}$ ) of the warm gas and it is likely that a significant amount of this metal-rich gas is dispersed to mix with other lower metallicity warm gas in the metallicity range ( $Z \sim 0.003$  to  $0.3 Z_{\odot}$ ). More importantly here, a significant amount of warm, metal-rich gas is heated to the WHIM temperature range, accounting for the differences seen at  $Z \sim 0.01$  to  $1.0 Z_{\odot}$  between the simulations without and with GSW shown in the middle panel of Figure 15. At the same time, it is also clearly seen that some of the WHIM gas at low metallicity ( $Z \leq 0.01 Z_{\odot}$ ) is substantially enriched and hence removed from that section and added to the section with  $Z \geq 0.01 Z_{\odot}$ . We find that the median metallicity of the WHIM is  $0.18 Z_{\odot}$  for oxygen with 50% and 90% intervals being (0.040,0.38) and (0.0017,0.83). Finally, the effect of GSW on

hot, cluster X-ray gas is rather minimal, as shown in the bottom panel of Figure 15. The metallicity of the cluster gas is robustly peaked at  $Z \sim 0.3 Z_{\odot}$  in terms of iron abundance, as observed (Arnaud et al. 1994; Tamura et al. 1996; Mushotzky et al. 1996; Mushotzky & Lowenstein 1997; Tozzi et al. 2003); in fact, this is how we normalize our metal yield (the sole parameter to determine the amount of metal output from stars) in order to construct a self-consistent picture. In our simplest, one-parameter model for metal yield, there is no adjustable free parameter that can alter the distribution of metals and our predictions as presented in the next section are completely deterministic and falsifiable.

Figure 16 shows the cumulative metal mass fraction as a function of gas density for each of the three IGM components. Overall, we find that in the simulation without GSW, (36%, 48%, 16%) of all metals in IGM are in the (warm, WHIM, hot) components. The distribution among the IGM components is altered to (warm, WHIM, hot)= (12%, 71%, 17%) in the simulation with GSW. This shows the GSW reduces the metal mass in the warm IGM component by a factor of 3!, while the hot IGM component is virtually unaffected by GSW. All the metals when a part of the warm IGM component heated up are added to the WHIM component. *This is the most dramatic effect that GSW have on one single physical component/process.* Also quite clear from the top panel of Figure 16, most of the metals that are heated and removed from the warm component are in relatively overdense regions, at  $\rho_{gas} \geq 200$ . However, most of the metals that are added to the WHIM are seen, from the middle panel of Figure 16, to be in regions spanning a significant range in density from 1 – 300 times the mean density. At the same time, as the middle panel of Figure 16 indicates, some WHIM gas in high density region ( $\rho > 300$ ) is affected in the opposite sense that their metallicity appears to be reduced by GSW (that the thick solid curve falls below the thin solid curve); however, a more correct interpretation is that the thin solid curve is pushed to the left to become the thick solid curve, i.e., GSW reduce gas density of this already metal-rich gas which is located in the very close vicinity

of galaxies.

Figure 17 further illustrates the effect of GSW on metal transport in a “phase” space, where we show *average* gas metallicity in the density-temperature phase space for the simulations with (top panel) and without (bottom panel) GSW. Let us examine them closely. First, in the bottom panel, we see a concentration of high metallicity gas ( $Z \geq Z_{\odot}$ ) at  $(\rho, T) = (> 10^4, \sim 10^4 \text{ K})$ , within the black contours which clearly is the gas within the galaxy that has been enriched by metals but remains cold-warm in the absence of GSW shocks. We note that the original gravitational shocks caused the gas to cool and condense to that phase space domain. Then in the upper panel this contour has vanished, this concentration of high-metallicity gas is essentially “blown away” by the GSW, as there remains little high metallicity gas in that phase space domain in the simulation with GSW (top panel). but in the upper panel this gas reappears at low density and high temperature within the black contour in the lower left corner. Specifically, as GSW propagate to lower density regions (cf. Figures 4,5,6), the metals transported there weigh relatively more importantly than in high density regions, creating high metallicity gas there. We see that in the WHIM temperature range of  $10^{5-7} \text{ K}$  there is a concentration of solar metallicity gas in the density range of 1 – 30 times the mean density, which can be easily probed by metal absorption line observations (see Cen & Fang 2005). We note that what is displayed here is the average metallicity and there is a very large dispersion in metallicity for gas elements in the same phase space location. Third, a significant fraction of WHIM gas in moderate to high density regions of  $\rho = 50 - 10^5$  is now significantly enriched to an average metallicity of  $0.1 - 0.3 Z_{\odot}$ .

From these results we expect that one of the most sensitive tests of GSW effect may lie in the properties of metal rich gas in the vicinity of galaxies and groups of galaxies, where density ranges from moderate to high and GSW are most energetically relevant.

These dramatic effects caused only by GSW, *not gravitational shocks*, can then be used to provide important tools to understand the GSW. Observationally, we expect metal lines, both metal absorption and emission lines, may serve as an excellent diagnostic for probing GSW, as will be shown in a later section. The absorption lines may be most efficient to probe the moderate density regions, while the emission lines may mostly concentrate on the high density regions.

#### 4. Discussion and Conclusions

Numerical simulations of the intergalactic medium have shown that at the present epoch a significant fraction (40 – 50%) of the baryonic component should be found in the ( $T \sim 10^5\text{--}7\text{K}$ ) Warm-Hot Intergalactic Medium (WHIM) - with several recent observational lines of evidence indicating the validity of the prediction. We here recompute the evolution of the WHIM with the following major improvements: (1) galactic superwind feedback processes from galaxy/star formation are explicitly included; (2) major metal species (O IV to O IX) are computed explicitly in a non-equilibrium way; (3) mass and spatial dynamic ranges are larger by a factor of 8 and 2, respectively, than our previous simulations.

Our significantly improved simulations confirm previous conclusions based on earlier simulations: *nearly one half of all baryons at the present epoch should be found in the WHIM* - a filamentary network in the temperature range of  $10^5 - 10^7$  K.

Here are the major findings: (1) Overall, the fraction of baryons in WHIM is slightly increased from the earlier work but consistent with the fraction at  $\sim 40 - 50\%$ . (2) galactic superwinds have three significant effects, first by increasing the WHIM mass fraction by about 20%, through shock heating photoionized gas adjacent to filaments, second by contaminating nearby gas with extra metals and additional heating, and third by dispersing

much of the metals within galaxies. (3) the gas density of the WHIM is broadly peaked at a density 10 – 20 times the mean density ranging from underdense regions to regions overdense by  $10^3 - 10^4$ . (4) the median metallicity of the WHIM is  $0.18 Z_{\odot}$  for oxygen with 50% and 90% intervals being  $(0.040, 0.38) Z_{\odot}$  and  $(0.0017, 0.83) Z_{\odot}$ .

The physics behind this robust conclusion is largely dictated by the dominance of gravitational heating when large-scale structures begin to collapse in the recent past in the cosmic history. Simply put, the average temperature of the intergalactic medium at any epoch is determined by the mass scale that goes nonlinear at that epoch, which, in present time, is close to the  $8h^{-1}\text{Mpc}$  scale which fixes the abundance of rich clusters. This explains the relative insensitivity of the computed mass fraction in the WHIM on cosmological parameters, so long as each model is properly normalized to reproduce the well determined abundance of observed rich clusters of galaxies today; only a very small extrapolation is needed to go from this well observed scale to the nonlinear scale, so the estimated temperature of collapsed regions that we find will be common to all models based on the gravitational growth of structure - as normalized to local cluster observations.

It was not entirely clear how important feedback processes from galaxy formation on IGM are, based on our early simulations compared to the simulations by others (Davé et al. 2001). In this work we demonstrate quantitatively, for the first time, this effect. We find that galactic superwinds generated collectively by supernova explosions in galaxies, while still subdominant to gravitational heating of large-scale structure formation, have important effects on the WHIM as well as other components of the IGM. The mass fraction of the WHIM is increased by about 20%, when GSW are included. We show that this increase in the WHIM mass fraction comes largely at the expense of the warm IGM phase over a broad range  $30 - 10^4$  times the mean density, which is often independently invoked to suppress star formation to alleviate the overcooling problem. A perhaps more important

effect of GSW is to transport metals to the IGM from inside galaxies to a distance of several hundred kiloparsecs up to about one megaparsec, a necessary process to enrich the IGM. It is therefore likely that detailed, joint analyses and comparisons with observations of the detailed structure of the WHIM density, temperature and metal abundances should be able to provide useful information on the GSW, which currently can only be modeled crudely. Nevertheless, with the adopted approximate treatment of GSW, we are able to show the significant effects on many observables, including the properties of major absorption lines and emissions lines in UV and soft X-ray.

We thank Taotao Fang, Ed Jenkins and Mike Shull for useful comments. The simulations were performed at the Pittsburgh Supercomputer Center. We thank R. Reddy at the Pittsburgh Supercomputer Center for constant and helpful assistance in the process of making the simulations. This work is supported in part by grants NNG05GK10G and AST-0507521.

## REFERENCES

- Arnaud, M., & Raymond, J. 1992, *ApJ*, 398, 394
- Arnaud, K. A., et al. 1994, *ApJ*, 436, L67
- Arnaud, M., & Rothenflug, R. 1985, *A&AS*, 60, 425
- Baumgartner, W.H., Loewenstein, M., Horner, D.J., Mushotzky, R.F. 2005, *ApJ*, 620, 680
- Bolton, J.S., Haehnelt, M.G., Viel, M., & Springel, V. 2005, *MNRAS*, 357, 1178
- Cen, R. 1992, *ApJS*, 78, 341
- Cen, R. 2003, *ApJ*, 591, 12
- Cen, R., & McDonald, P. 2002, *ApJ*, 570, 457
- Cen, R. & Ostriker, J. P. 1999, *ApJ*, 519, L109, “CO”.
- Cen, R., Nagamine, K., & Ostriker, J.P. 2005, *ApJ*, in press
- Cen, R. Tripp, T.M., Ostriker, J.P., & Jenkins, E.B. 2001, *ApJ*, 559, L5.
- Chen, X., Weinberg, D.H., Katz, N., & Davé, R. 2003, *ApJ*, 594, 42
- Clark, R. E. H., Cowan, R. D., & Bobrowicz, F. W. 1986, *Atomic Data and Nuclear Data Tables*, 34, 415
- Dupke, R.A., & Anaud, K.A. 2001, *ApJ*, 548, 141
- Dupke, R.A., & White, R.E., III 2000, *ApJ*, 537, 123
- Elizondo, D., Yepes, G., Kates, R., Muller, V., & Klypin, A. 1999a, *ApJ*, 515, 525
- Elizondo, D., Yepes, G., Kates, R., & Klypin, A. 1999b, *NewA*, 4, 101

- Ettori, S. 2005, MNRAS, 362, 110
- Fan, X., et al. 2002, AJ, 123, 1247
- Fang, T., Davis, D.S., Lee, J.C., Marshall, H.L., Bryan, G.L., & Canizares, C.R. 2002a, ApJ, 565, 86
- Fang, T., Marshall, H.L., Lee, J.C., Davis, D.S., & Canizares, C.R. 2002b, ApJ, 527, L127
- Fang, T., Sembach, K.R., & Canizares, C.R. 2003, ApJ, 586, L49
- Fang, T., Croft, R. A. C., Sanders, W. T., Houck, J., Davé, R., Katz, N., Weinberg, D. H., & Hernquist, L. 2005, ApJ, 623, 612
- Fang, T., & Bryan, G. L. 2001, ApJ, 564, L31
- Fang, T., Bryan, G. L., & Canizares, C. R. 2002, ApJ, 564, 604
- Ferland, G. J., Korista, K. T., Verner, D. A., Ferguson, J. W., Kingdon, J. B., & Verner, E. M. 1998, PASP, 110, 761
- Finoguenov, A., Briel, U.G., & Henry, J.P. 2003, A& A, 410, 777
- Fukugita, M., Hogan, C.J., & Peebles, P.J.E. 1998, ApJ, 503, 518
- Furlanetto, S.R., Schaye, J., Springel, V., & Hernquist, L. 2004, ApJ, 606, 221
- Furlanetto, S.R., Schaye, J., Springel, V., & Hernquist, L. 2005a, ApJ, 622, 7
- Furlanetto, S.R., Phillips, L.A., & Kamionkowski, M. 2005b, MNRAS, 359, 295
- Gnedin, N.Y., & Ostriker, J.P. 1997, ApJ, 486, 581
- Haardt, F., & Madau, P. 1999, ApJ, 514, 648
- Hultman, J., & Pharasyn, A. 1999, A&A, 347, 769



- Kaastra, J.S., Lieu, R., Tamura, T., Paerels, F.B.S., & den Herder, J.W. 2003, *A& A*, 397, 445
- Kormendy, J., & Gebhardt, K. 2001, 20th Texas Symposium on relativistic astrophysics, AIP conference proceedings, Vol. 586. Edited by J. Craig Wheeler and Hugo Martel, p.363
- Mathur, S., Weinberg, D.H., & Chen, X. 2003, *ApJ*, 582, 82
- Mushotzky, R. F., & Lowenstein, M. 1997, *ApJ*, 481, L63
- Mushotzky, R. F., Lowenstein, M., Arnaud, A. K., Tamura, T., Fukazawa, Y., Matsushita, K., Kikuchi, K., & Hatsukade, I. 1996, *ApJ*, 466, 686
- Nicastro, F., et al. 2005, *Nature*, 433, 495
- Oegerle, W.R., et al. 2000, *ApJ*, 538, L20
- Peebles, P.J.E. 1999, preprint, astro-ph/9910234
- Penton, S.V., Stocke, J.T., & Shull, J.M. 2004, *ApJS*, 152, 29
- Portinari, L., Moretti, A., Chiosi, C., & Sommer-Larsen, J. 2004, *ApJ*, 604, 579
- Rauch, M. et al. 1997, *ApJ*, 489, 7
- Ricotti, M., & Ostriker, J.P. 2004, *MNRAS*, 350, 539
- Ritchie, B. W., & Thomas, P. A. 2001, *MNRAS*, 323, 743
- Sembach, K.R., Tripp, T.M., Savage, B.D., & Richter, P. 2004, *ApJS*, 155, 351
- Savage, B.D., Sembach, K.R., Tripp, T.M., & Richter, P. 2002, *ApJ*, 564, 631
- Scharf, C., Donahue, M., Voit, G.M., Rosati, P., & Postman, M. 2000, *ApJ*, 528, L73

- Shull, J. M., Tumlinson, J., & Giroux, M. L. 2003, *ApJ*, 594, L107
- Shull, J. M., & van Steenberg, M. 1982, *ApJS*, 48, 95
- Shull, J. M., et al. 1999, *AJ*, 118, 1450
- Shapley, A.E., et al. 2005, in preparation.
- Springel, V., & Hernquist, L. 2003, *MNRAS*, 339, 289
- Steidel, C.C., Pettini, M., & Adelberger, K.L. 2001, *ApJ*, 546, 665
- Stocke, J.T., Penton, S.V., Danforth, C.W., Shull, J.M., Tumlinson, J., & McLin, K.M.  
2005, astro-ph/0509822
- Tamura, T., et al. 1996, *PASP*, 48, 671
- Tamura, T., et al. 2004, *A&A*, 420, 135
- Tegmark, M., et al. 2004, *Phy. Rev. D*, 69, 103501
- Tittley, E.R., & Henriksen, M.J. 2001, *ApJ*, 563, 673
- Tozzi, P., Rosati, P., Ettori, S., Borgani, S., Mainieri, V., & Norman, C. 2003, *ApJ*, 593,  
705
- Tripp, T. M., Savage, B. D. & Jenkins, E. B. 2000, *ApJ*, 534, L1
- Tripp, T. M., & Savage, B. D. 2000, *ApJ*, 542, 42
- Tsujimoto, T., Nomoto, K., Yoshii, Y., Hashimoto, M., Yanagida, S., & Thielemann, F.-K.  
1995, *MNRAS*, 277, 945
- Verner, D. A., & Ferland, G. J. 1996, *ApJS*, 103, 467
- Verner, D. A., Ferland, G. J., Korista, K. T., & Yakovlev, D. G. 1996, *ApJ*, 465, 487

Voronov, G. S. 1997, *Atomic Data and Nuclear Data Tables*, 65, 1

Yepes, G., Kates, R., Khokhlov, A., & Klypin, A. 1997, *MNRAS*, 284, 235

Yoshikawa, K., et al. 2003, *PASJ*, 55, 879

Yoshikawa, K., et al. 2004b, *PASJ*, 56, 939

Yu, Q., & Tremaine, S. 2002, *MNRAS*, 335, 965

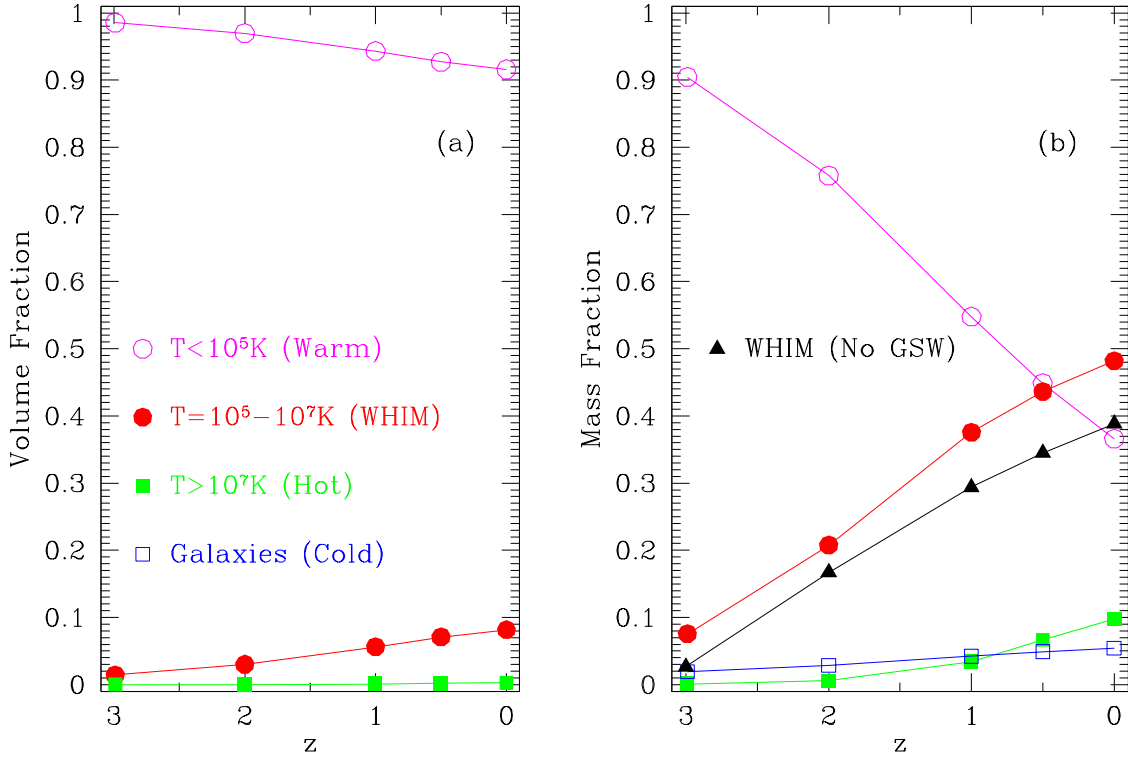


Fig. 1.— shows the evolution of the four components of cosmic baryons (see text for definitions) for the simulation with GSW. Panel (a) shows the volume fractions of the four components and panel (b) shows the mass fractions. Examination of (b) shows that about one half of all baryons at redshift zero are in the WHIM. Also included in Panel (b) as solid triangles is the mass evolution of the WHIM from the simulation with no GSW.

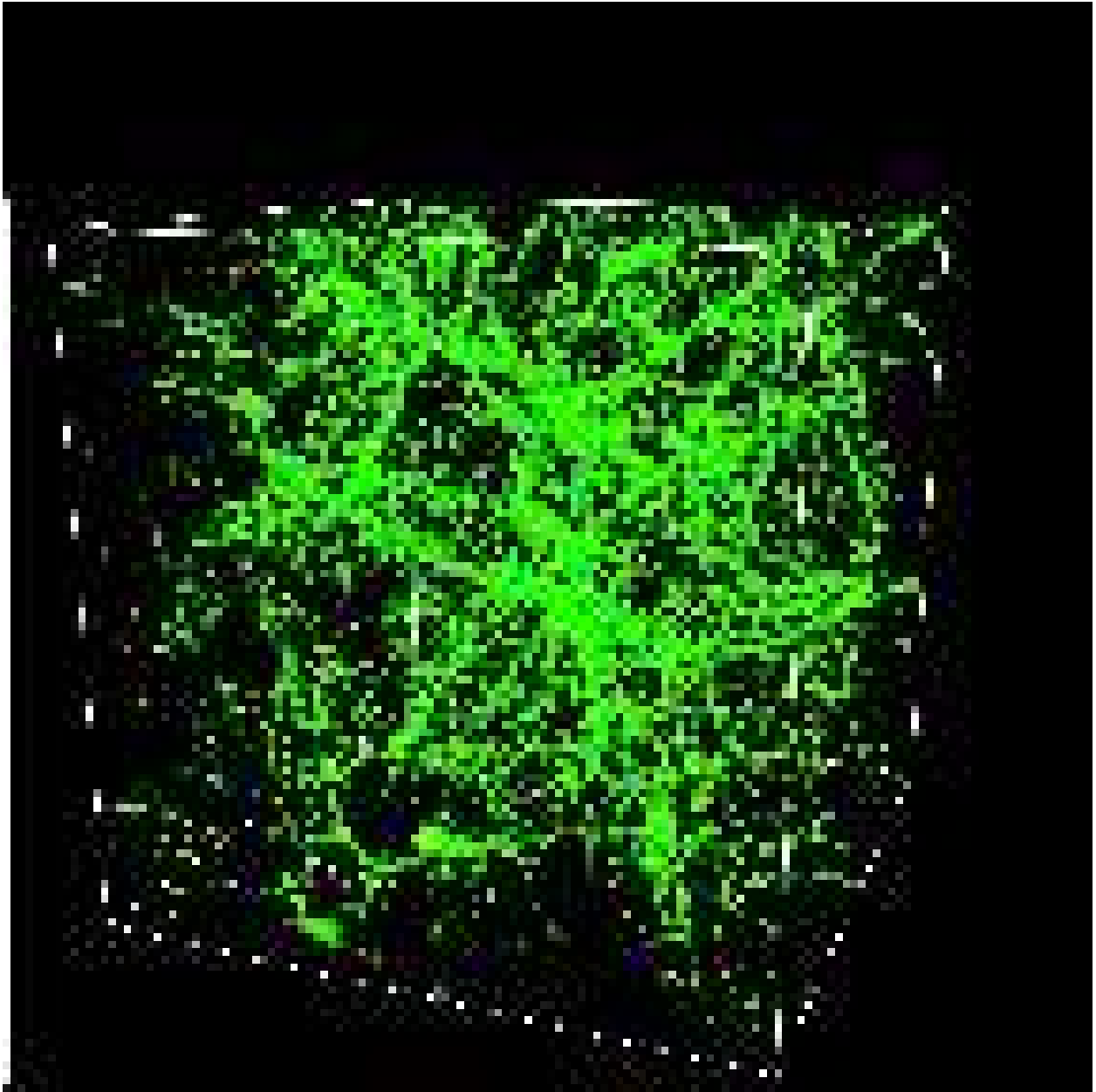


Fig. 2.— shows the spatial distribution of the warm/hot gas with temperature in the range  $10^5\text{--}7\text{K}$  at  $z = 0$  in a box of size  $85h^{-1}\text{Mpc}/h$  containing  $10^9$  individual cells, showing the characteristic appearance of a “Cosmic Web”. The green regions have densities about 10–20 times the mean baryon density of the universe at  $z = 0$ ; the yellow regions have densities about one hundred times the mean baryon density, while the small isolated regions with red and saturated dark colors have even higher densities reaching about a thousand times the mean baryon density, and are sites for current galaxy formation.

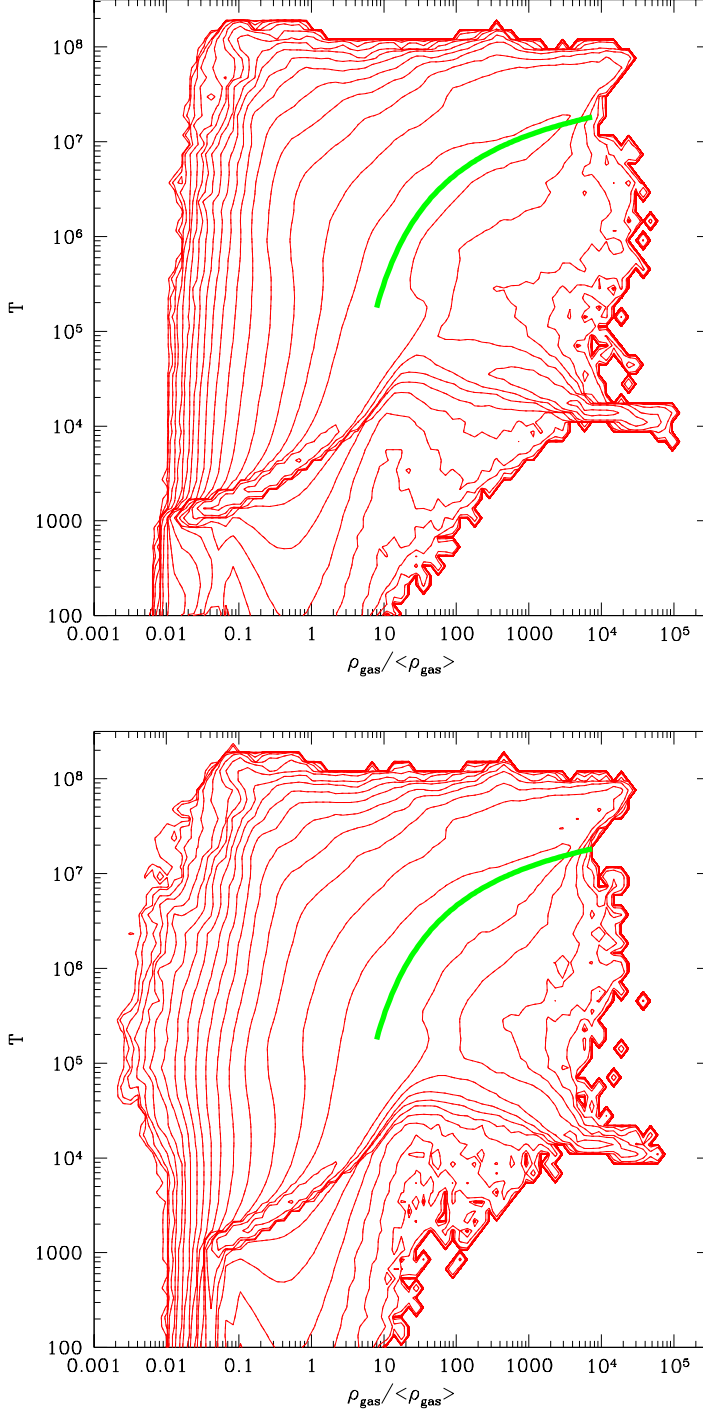


Fig. 3.— shows the concentration of (all) gas mass in the density-temperature plane for the run without galactic superwinds (top panel) and with (bottom panel). The thick solid curve is a fitting formula tracing the locus for the WHIM ridge line (see Equation 1 in text). There are two contour levels per decade.

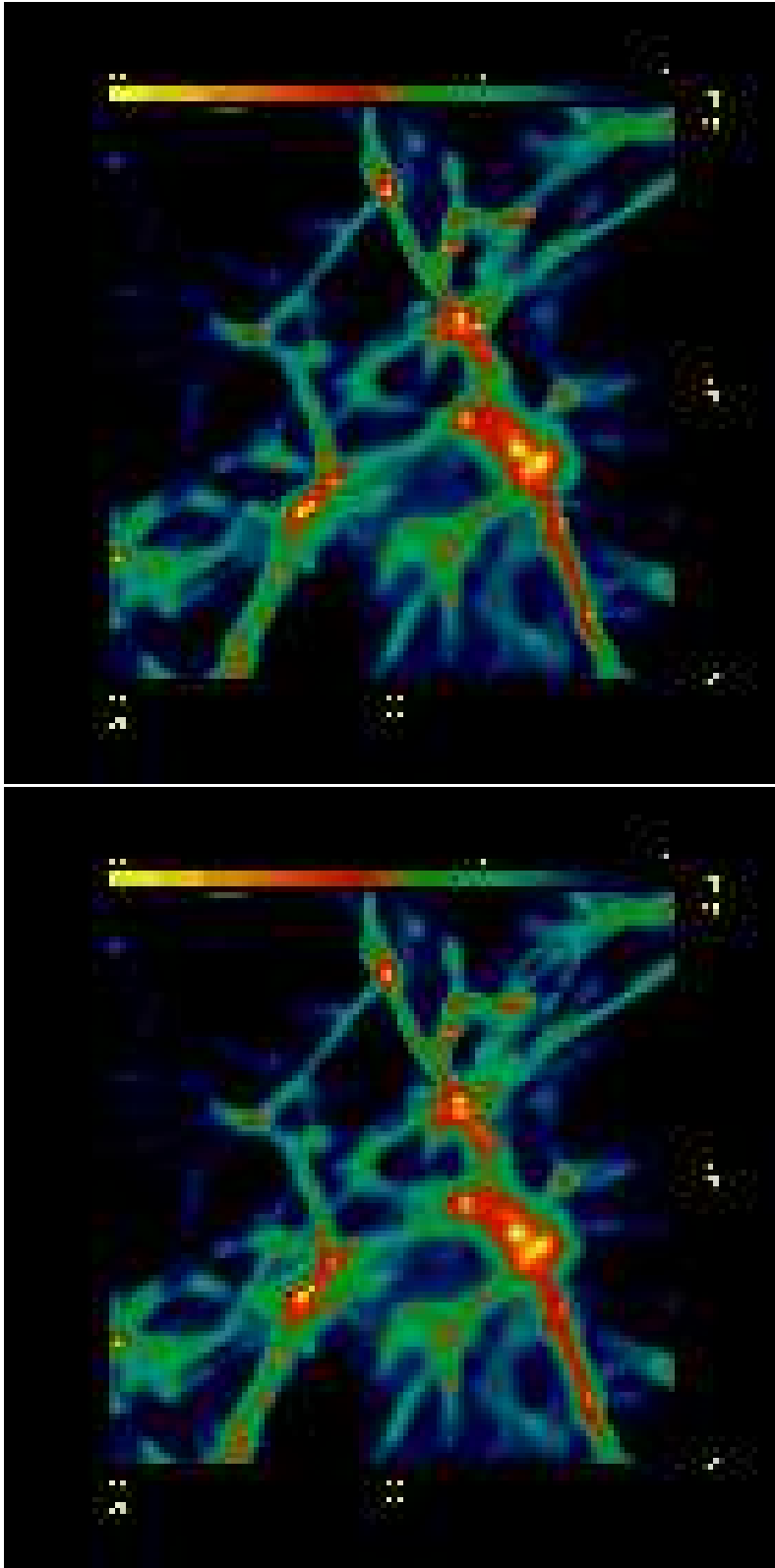


Fig. 4.— shows the spatial distribution of  $\log(\rho)_{gas}$  in a thin slice of size  $21.2 \times 21.2 \text{Mpc}^2/h^2$  and depth  $1.75 \text{Mpc}/h$  without (top) and with (bottom) GSW. Note that gas of all temperatures is included in this plot. Note reduction of yellow high density regions as GSW push gas out to lower densities. Visible examples include the features at  $(8, 5) \text{Mpc}/h$ ,  $(13, 8) \text{Mpc}/h$  and  $(6, 13) \text{Mpc}/h$ .

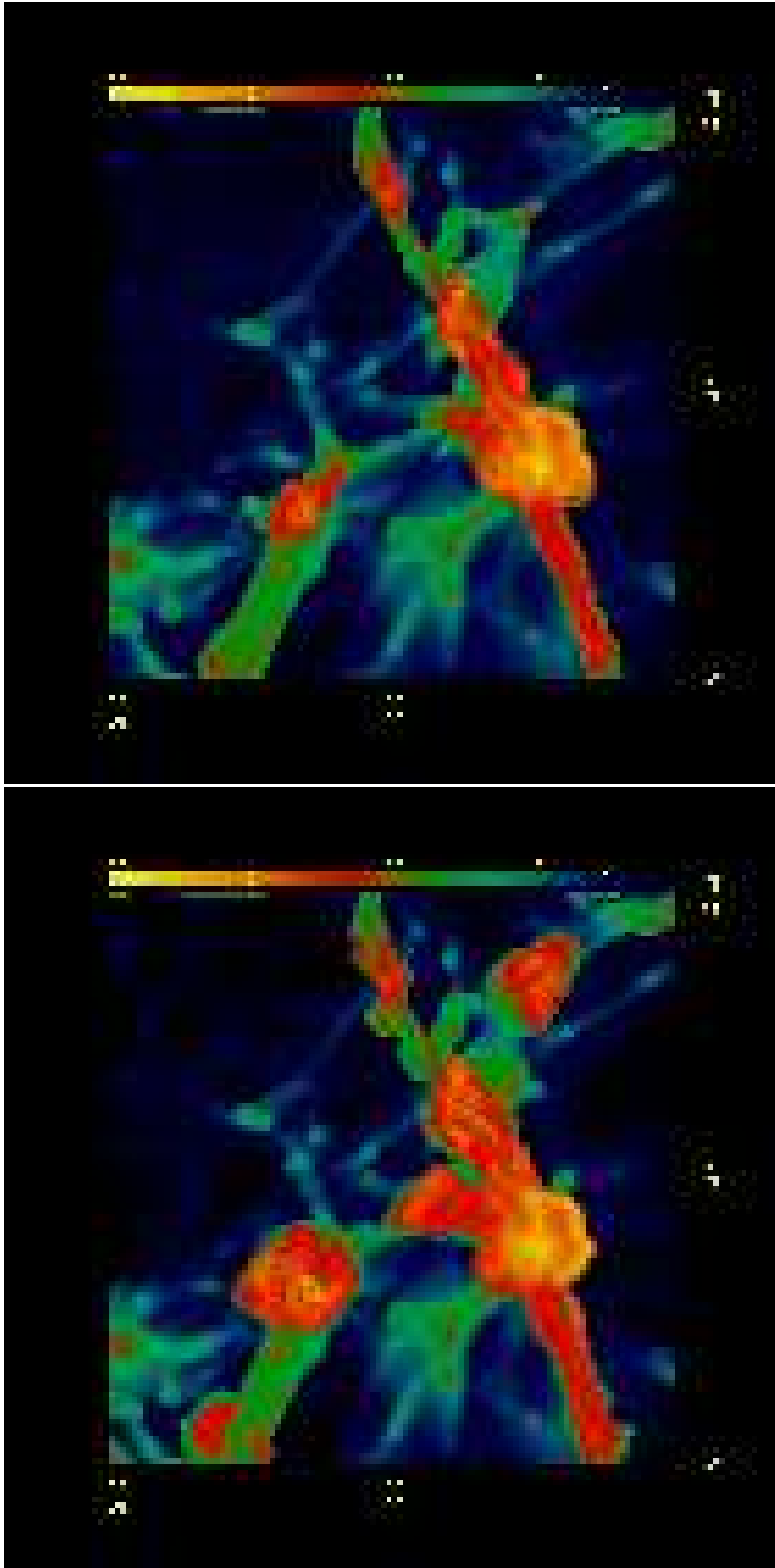


Fig. 5.— shows the spatial distribution of  $\log(\text{gas temperature})$  in the same slice without (top) and with (bottom) GSW. The temperature is units of Kelvin. Note shocked spurs propagating perpendicular to filaments.



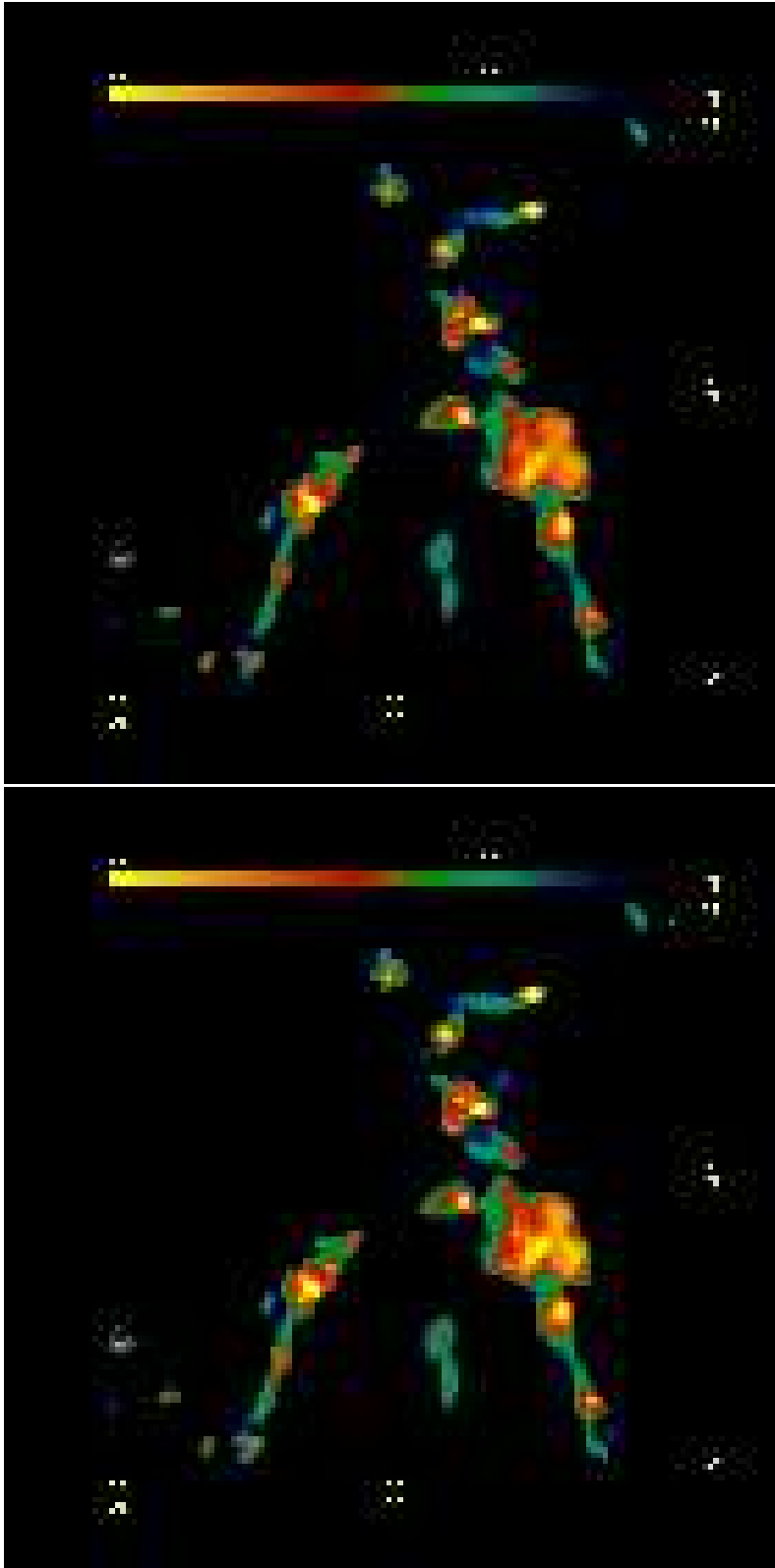


Fig. 6.— shows the spatial distribution of  $\log(\text{metal density})$  in the same slice without (top) and with (bottom) GSW. The gas metallicity is in units of solar metallicity. Note slightly greater extent of metal rich regions with GSW.

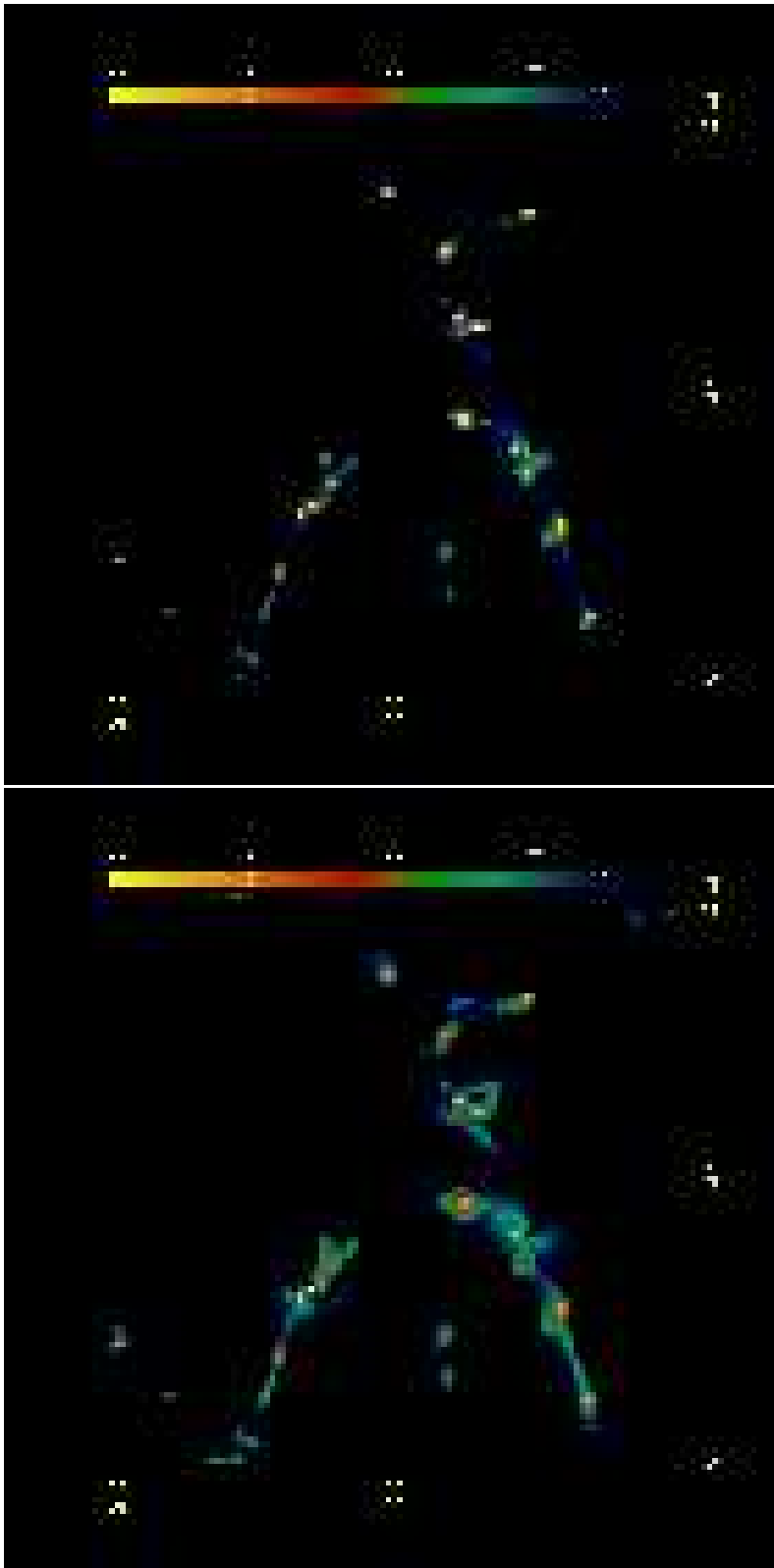


Fig. 7.— shows the spatial distribution of  $\log(\text{O VI density})$  in the same slice without (top) and with (bottom) GSW. The density is in units of the global mean gas density. Significantly greater volume of O VI reflects both temperature and metallicity effects of GSW.

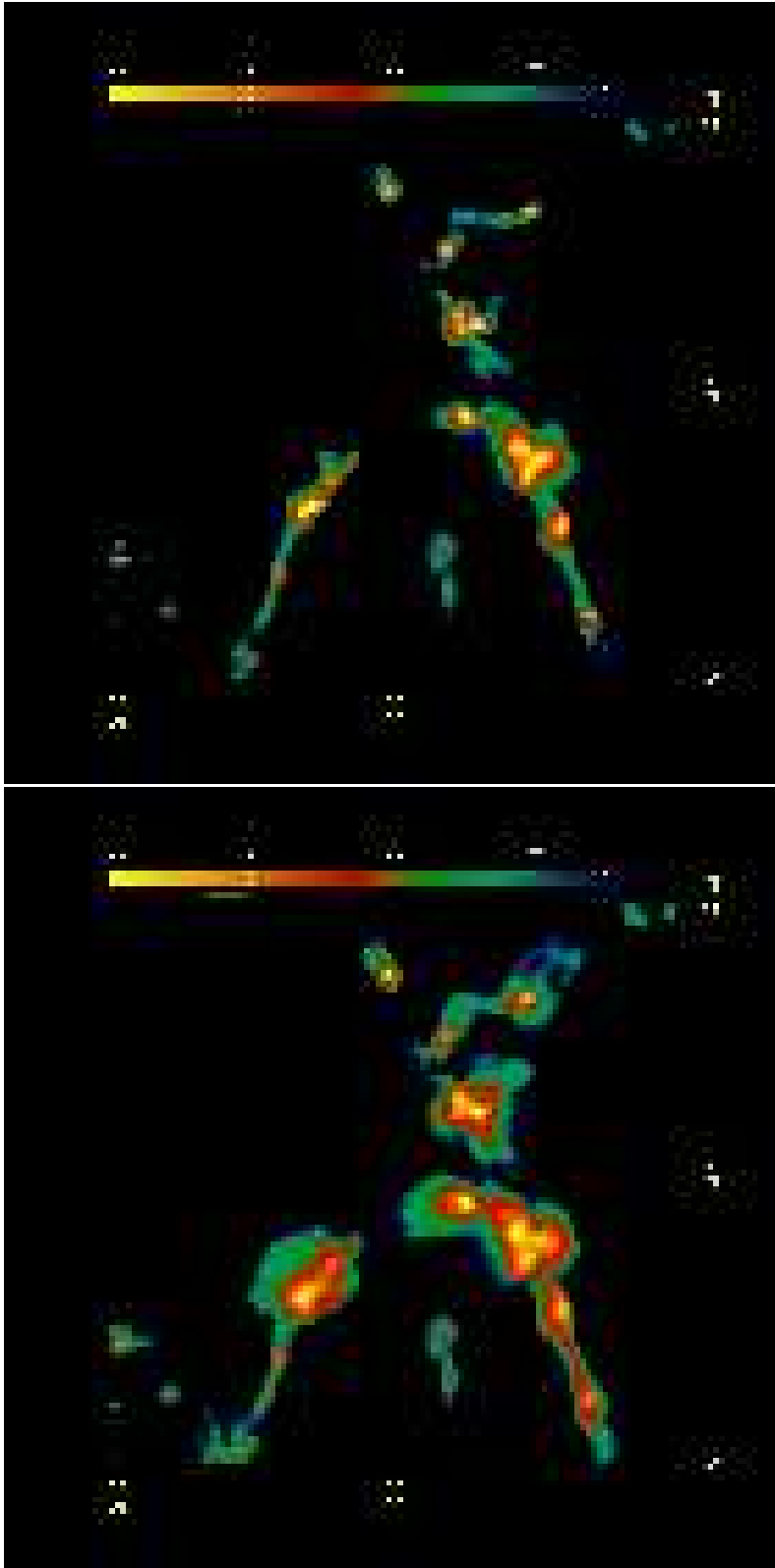


Fig. 8.— shows the spatial distribution of  $\log(\text{O VII density})$  in the same slice without (top) and with (bottom) GSW. The density is in units of the global mean gas density. GSW effects are stronger for O VII than O VI.

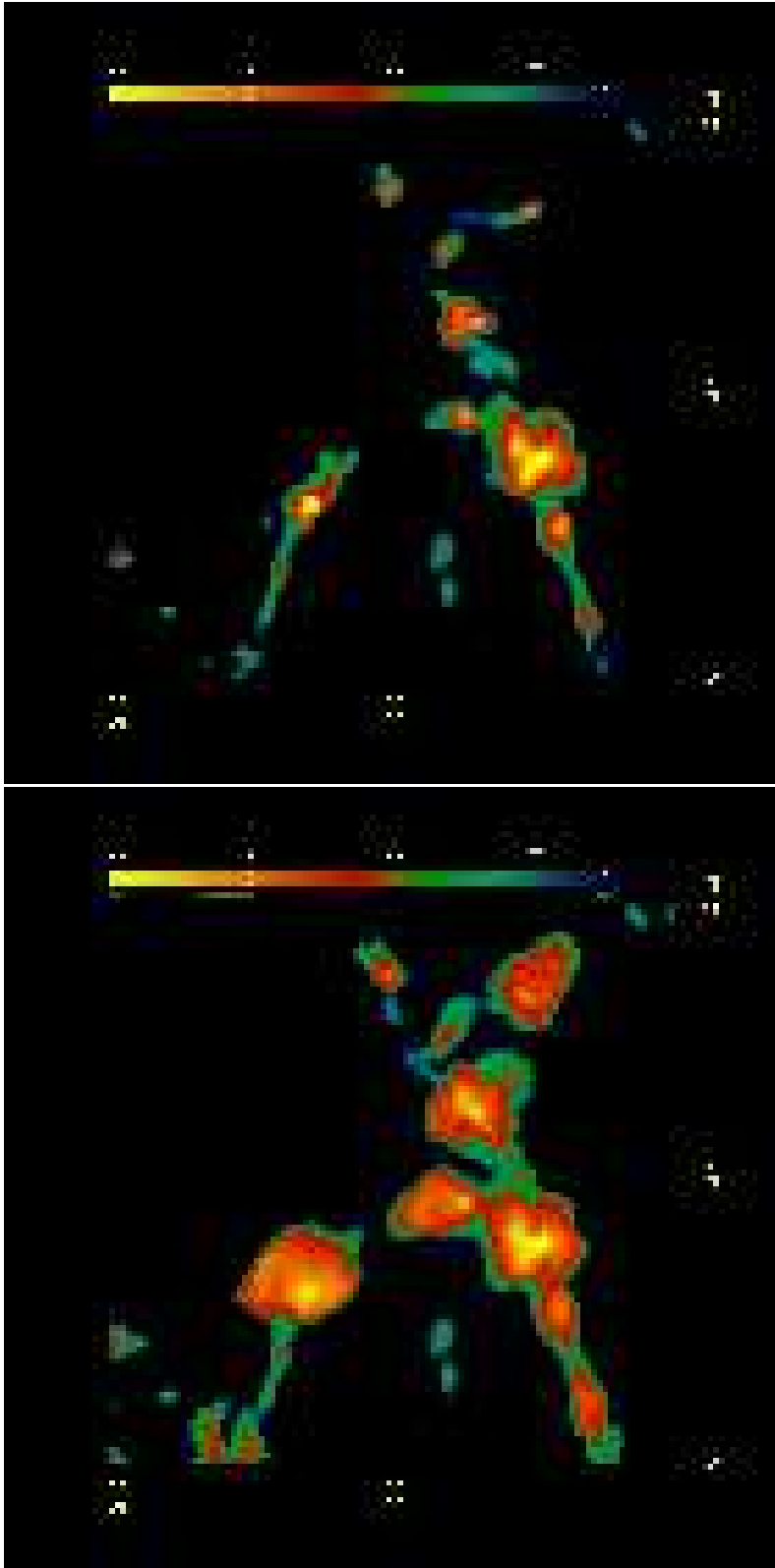


Fig. 9.— shows the spatial distribution of  $\log(\text{O VIII density})$  in the same slice without (top) and with (bottom) GSW. The density is in units of the global mean gas density. Here GSW effects on the prevalence of O VIII are seem to be dramatic.

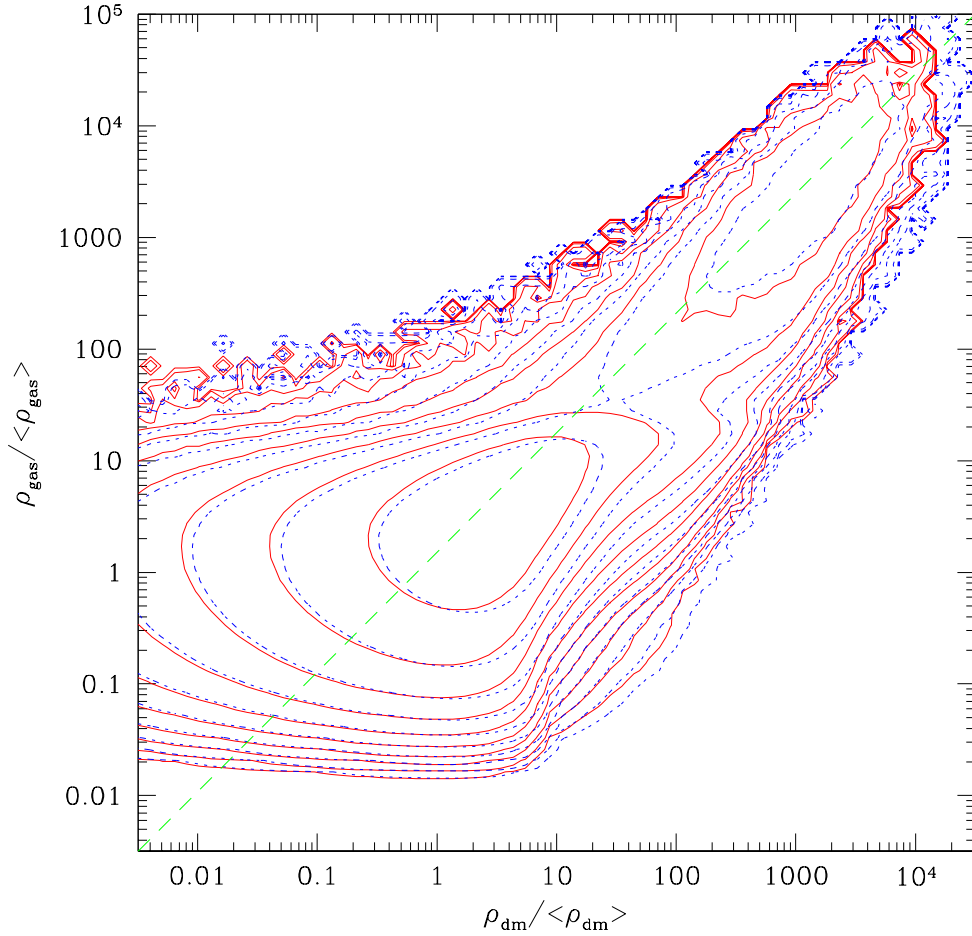


Fig. 10.— shows the mass concentration of cold gas ( $T < 10^5$  K) in the dark matter density-gas density plane for the simulation with galactic superwinds (red solid contours) and that without galactic superwinds (blue dotted contours). Both dark matter density and gas density are in units of their respective mean density. There are two contour levels per decade.

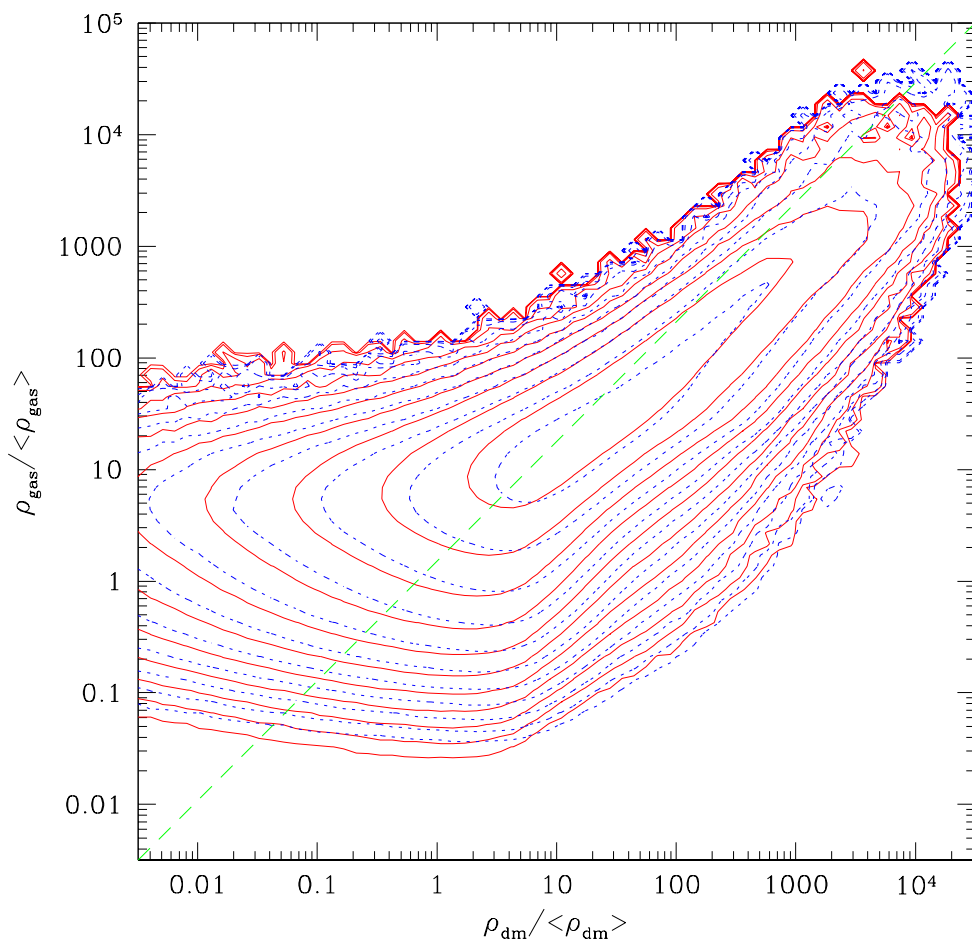


Fig. 11.— shows the mass concentration of the WHIM gas ( $T = 10^{5-7}$  K) in the dark matter density-gas density plane for the simulation with galactic superwinds (red solid contours) and that without galactic superwinds (blue dotted contours). Both dark matter density and gas density are in units of their respective mean density.

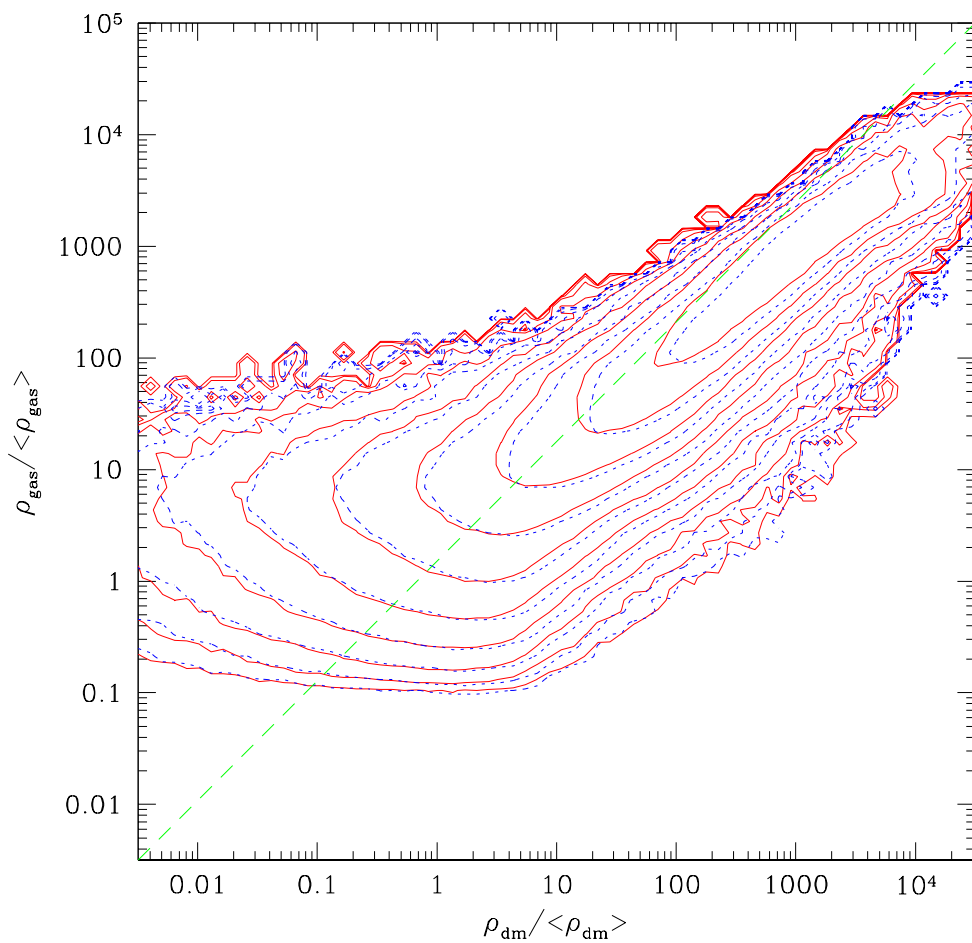


Fig. 12.— shows the mass concentration of the hot X-ray gas ( $T > 10^7$  K) in the dark matter density-gas density plane for the simulation with galactic superwinds (red solid contours) and that without galactic superwinds (blue dotted contours). Both dark matter density and gas density are in units of their respective mean density.

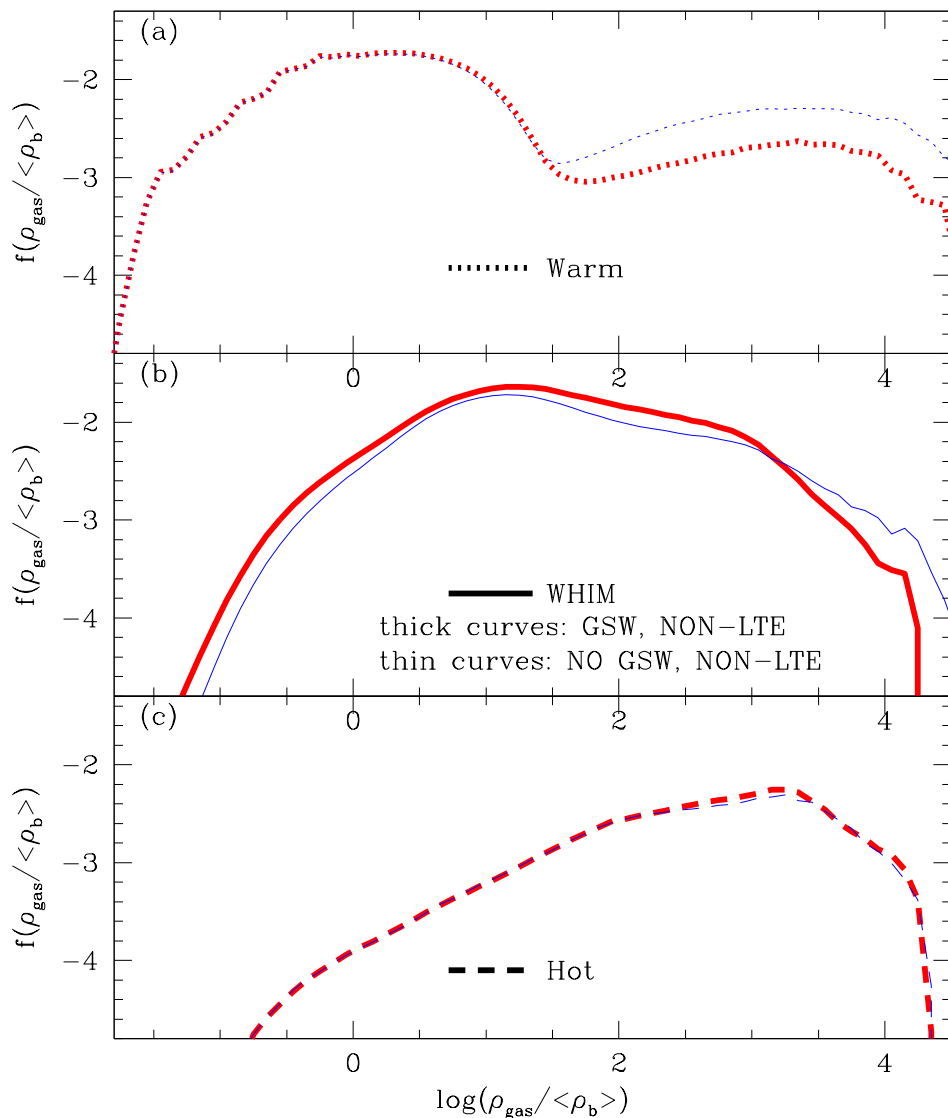


Fig. 13.— shows the differential mass fraction of three IGM components - warm gas (dotted), WHIM (solid) and hot gas (dashed) as a function of gas temperature for the simulation with galactic superwinds (thick curves) and that without galactic superwinds (thin curves). The primary effect of GSW is deplete high density warm gas near galaxies, pushing it to lower densities and higher temperatures.



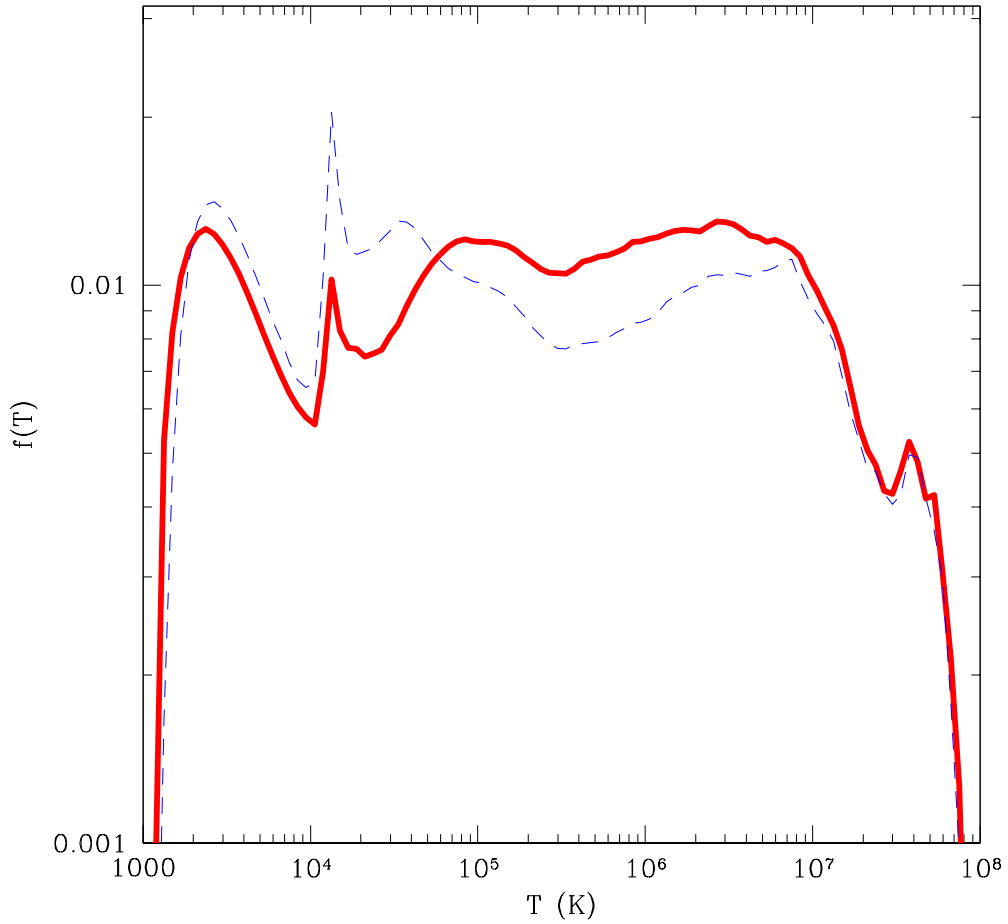


Fig. 14.— shows the differential mass fraction vs gas temperature for the simulation with galactic superwinds (thick solid curves) and that without galactic superwinds (thin dashed curves). We see how gas in the photoionized or warm peak at  $T \sim 1.5 \times 10^4$  K has been depleted and shock heated mostly into the  $10^{5-7}$  K range.

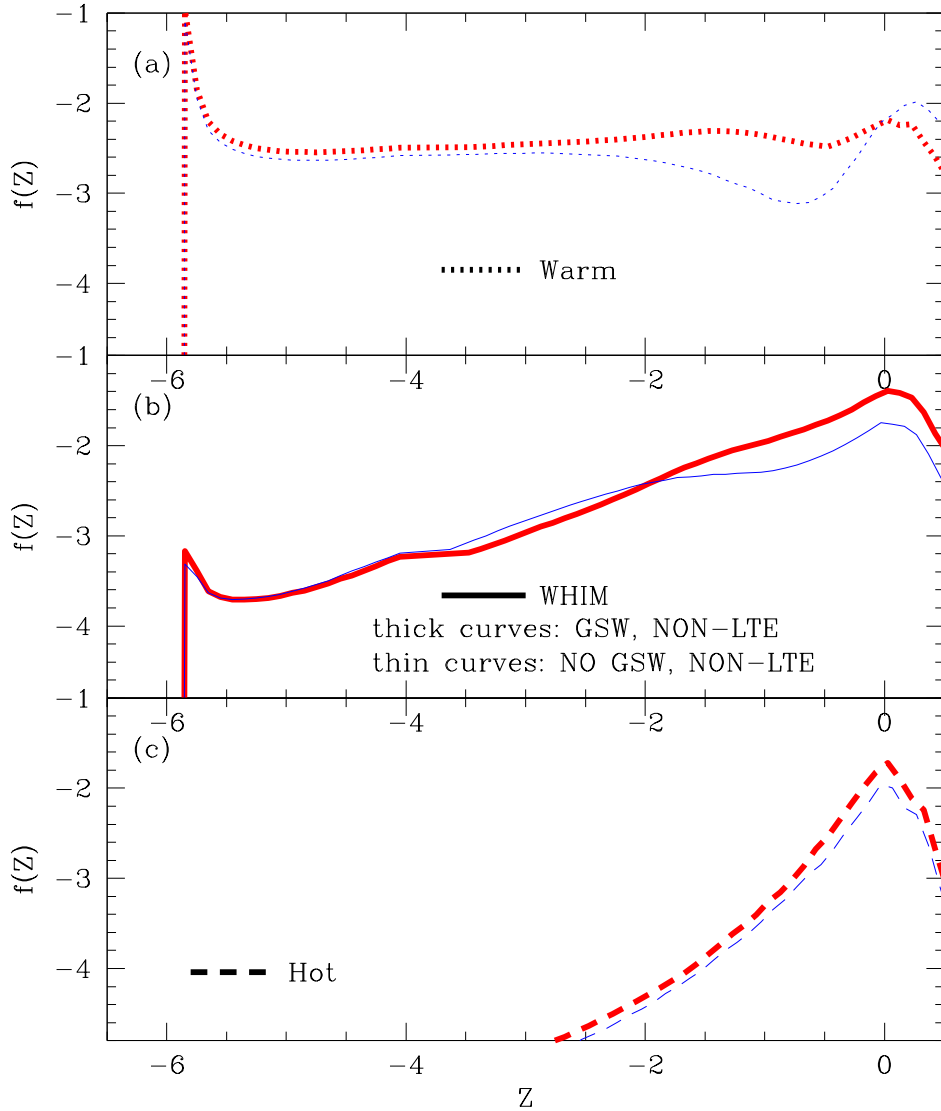


Fig. 15.— shows the differential mass fraction as a function of gas metallicity for the three IGM components for the simulation with galactic superwinds (thick curves) and that without galactic superwinds (thin curves). Metal rich gas in the warm component near galaxies has been shock heated to the WHIM state.

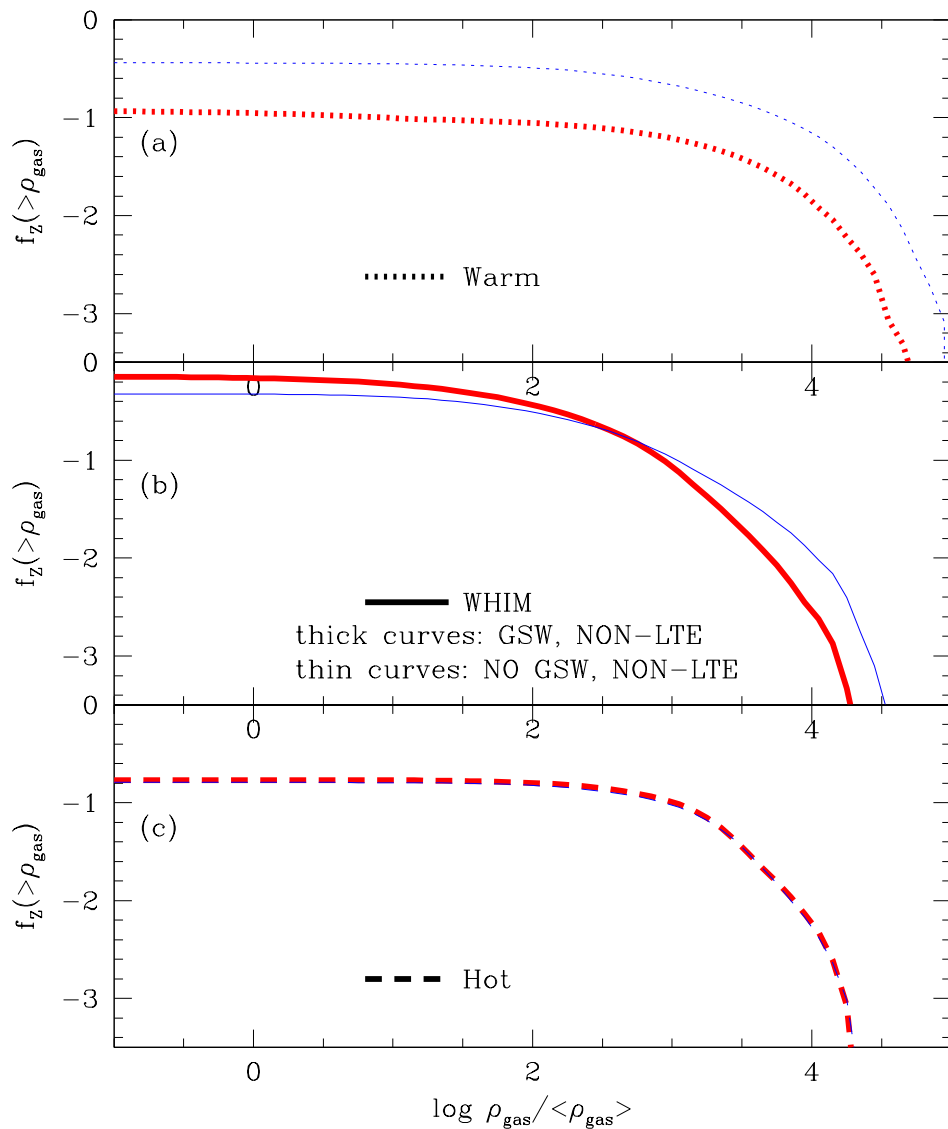


Fig. 16.— shows the cumulative metal mass fraction as a function of gas density (in units of mean gas density) for the three IGM components for the simulation with galactic superwinds (thick curves) and that without galactic superwinds (thin curves). Note that the sum of  $f_z(>0)$  for the three component is unity in each simulation.

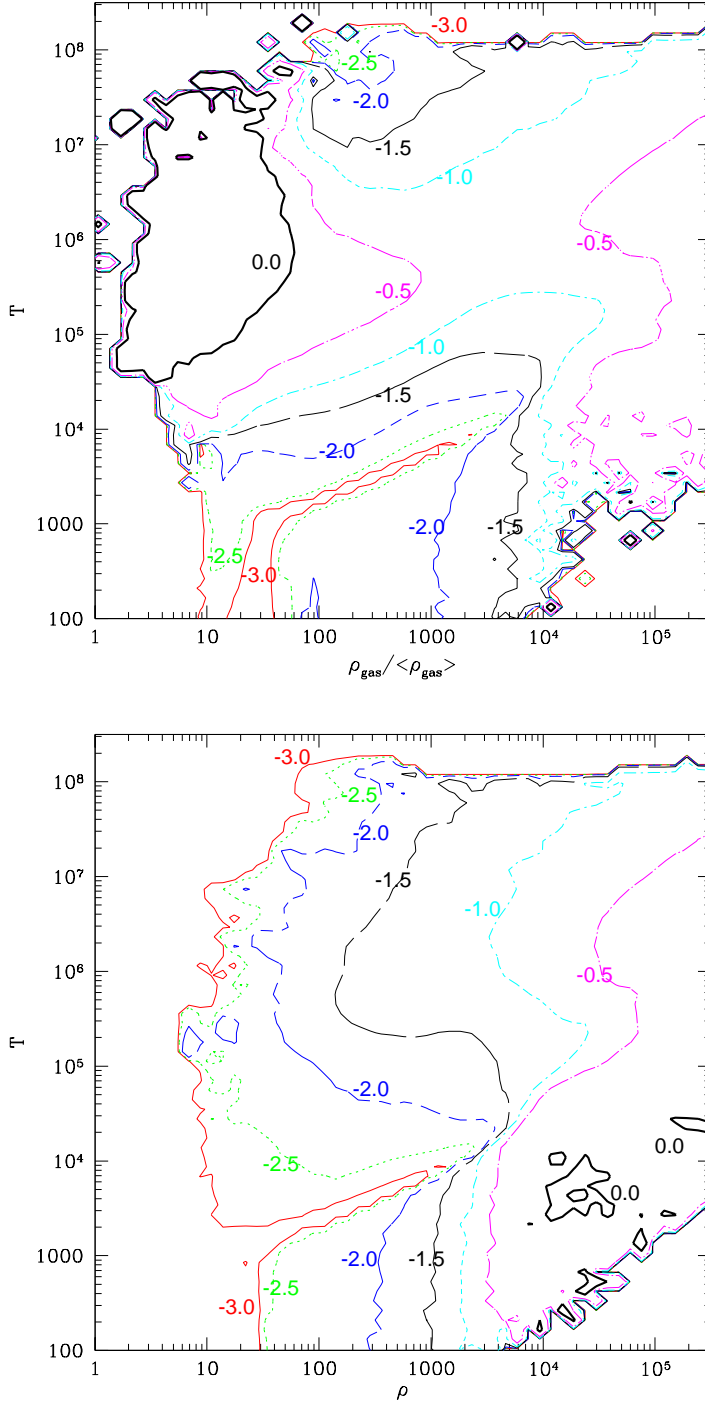


Fig. 17.— shows the average metallicity of gas in the density-temperature plane for the run with galactic superwinds (top panel) and without (bottom panel). The difference contours represent different metallicity levels, labeled by numbers in solar units. Specifically, the thin solid, dotted, dashed, long-dashed, dotted-dashed, dotted-long-dashed and thick solid